



# Measurements of the suppression and correlations of dijets in Pb+Pb collisions at $\sqrt{s_{\text{NN}}} = 5.02$ TeV

The ATLAS Collaboration

Studies of the correlations of the two highest transverse momentum (leading) jets in individual Pb+Pb collision events can provide information about the mechanism of jet quenching by the hot and dense matter created in such collisions. In Pb+Pb and  $pp$  collisions at  $\sqrt{s_{\text{NN}}} = 5.02$  TeV, measurements of the leading dijet transverse momentum ( $p_{\text{T}}$ ) correlations are presented. Additionally, measurements in Pb+Pb collisions of the dijet pair nuclear modification factors projected along leading and subleading jet  $p_{\text{T}}$  are made. The measurements are performed using the ATLAS detector at the LHC with  $260 \text{ pb}^{-1}$  of  $pp$  data collected in 2017 and  $2.2 \text{ nb}^{-1}$  of Pb+Pb data collected in 2015 and 2018. An unfolding procedure is applied to the two-dimensional leading and subleading jet  $p_{\text{T}}$  distributions to account for experimental effects in the measurement of both jets. Results are provided for dijets with leading jet  $p_{\text{T}}$  greater than 100 GeV. Measurements of the dijet-yield-normalized  $x_{\text{J}}$  distributions in Pb+Pb collisions show an increased fraction of imbalanced jets compared to  $pp$  collisions; these measurements are in agreement with previous measurements of the same quantity at 2.76 TeV in the overlapping kinematic range. Measurements of the absolutely-normalized dijet rate in Pb+Pb and  $pp$  collisions are also presented, and show that balanced dijets are significantly more suppressed than imbalanced dijets in Pb+Pb collisions. It is observed in the measurements of the pair nuclear modification factors that the subleading jets are significantly suppressed relative to leading jets with  $p_{\text{T}}$  between 100 and 316 GeV for all centralities in Pb+Pb collisions.

# Contents

<b>1</b>	<b>Introduction</b>	<b>2</b>
<b>2</b>	<b>ATLAS detector</b>	<b>5</b>
<b>3</b>	<b>Data and Monte Carlo selection</b>	<b>5</b>
<b>4</b>	<b>Jet reconstruction and performance</b>	<b>6</b>
<b>5</b>	<b>Data analysis</b>	<b>8</b>
<b>6</b>	<b>Systematic uncertainties</b>	<b>11</b>
<b>7</b>	<b>Results</b>	<b>13</b>
7.1	Dijet-yield-normalized $x_J$ distributions	13
7.2	Absolutely normalized $x_J$ distributions	14
7.3	$R_{AA}^{\text{pair}}$ of leading and subleading jets	16
<b>8</b>	<b>Conclusion</b>	<b>21</b>
	<b>Appendix</b>	<b>23</b>

## 1 Introduction

The principal physics aim of the heavy-ion program at the Large Hadron Collider (LHC) is to produce and measure the properties of the quark–gluon plasma (QGP). In quantum chromodynamics (QCD), the QGP is a high-temperature state of matter in which quarks and gluons are no longer confined in color-neutral hadrons such as protons and neutrons (for a recent review, see Ref. [1]). In order to understand the properties of the QGP at short distances, high transverse momenta ( $p_T$ ) probes such as jets of correlated particles are used.

The overall rate of jets in a given centrality<sup>1</sup> interval in Pb+Pb collisions at a given  $p_T$  is characterized by the nuclear modification factor,

$$R_{AA} = \frac{1}{N_{\text{evt}}} \frac{dN_{\text{jet}}}{dp_T} \bigg/ \left( \langle T_{AA} \rangle \frac{d\sigma_{pp}}{dp_T} \right), \quad (1)$$

where  $N_{\text{jet}}$  and  $\sigma_{pp}$  are the jet yield in Pb+Pb collisions and the jet cross-section in  $pp$  collisions, respectively, measured as a function of the jet  $p_T$ , and where  $N_{\text{evt}}$  is the total number of Pb+Pb events within the chosen centrality interval. Additionally,  $\langle T_{AA} \rangle$  is the mean nuclear thickness function [2] for the centrality interval. The  $R_{AA}$  value is one in the absence of nuclear effects, however in the most central Pb+Pb collisions,  $R_{AA}$  is observed to be about a factor of two lower than that in  $pp$  collisions scaled by

---

<sup>1</sup> Centrality characterizes the degree to which the nuclei overlap. The most central collisions have full overlap and the highest multiplicities, while the most peripheral collisions have only minimal overlap and have multiplicity closer to that in  $pp$  collisions at the same nucleon–nucleon collision energy.

$\langle T_{AA} \rangle$ , up to a  $p_T$  of approximately 1 TeV [3–5]. This suppression, referred to as *jet quenching*, is generally explained by the interplay of radiative and collisional energy loss in reducing the jet  $p_T$  by moving energy associated with the initial parton to wider angles, with some of it being outside the jet cone. Given the steeply falling jet  $p_T$  spectrum, this leads to fewer jets being measured at a given jet  $p_T$ , giving rise to  $R_{AA}$  values below one. For recent reviews, see Refs. [6, 7].

Jets are mostly produced in pairs in  $2 \rightarrow 2$  scattering processes. The QCD evolution of the initial partons gives rise to back-to-back jets, referred to here as “dijets”. Compared to single-jet suppression, dijets in Pb+Pb collisions provide a cleaner probe for studying jet quenching. The two jets are expected to experience asymmetric energy loss due to traversing unequal path lengths in the QGP [8], driven by the geometry of the overlapping nuclei and the relative orientation of the jet trajectories through the evolving medium. Measurements of the azimuthal anisotropy of jets [9] have already shown that the geometry of the overlapping nuclei affects the relative rates of jets measured in Pb+Pb collisions. Additionally, jets are expected to experience jet-by-jet fluctuations in the energy-loss process [10]. The measurement of the  $p_T$  balance of dijets provides a way to constrain the relative importance of fluctuations and geometry in jet quenching.

In order to compare the final transverse momenta of the two jets which define a dijet, the leading dijet momentum balance:

$$x_J \equiv p_{T,2}/p_{T,1} \quad (2)$$

is measured. Here, the leading dijet is constructed using the highest two  $p_T$  jets out of the set of jets in an event,  $p_{T,1}$  is the transverse momentum of the highest- $p_T$  (leading) jet, and  $p_{T,2}$  is the transverse momentum of the second-highest- $p_T$  (subleading) jet.

In  $pp$  collisions, the showering process in vacuum (in the absence of a significant QGP), as well as higher-order scattering processes, can lead to imbalanced dijet transverse momenta. However, the most probable situation is that the jets are nearly balanced in  $p_T$  [11]. Previous dijet measurements in Pb+Pb collisions have observed that jets are more likely to have a larger momentum imbalance in Pb+Pb collisions than in  $pp$  collisions [11–13].

Previous publications reported only the dijet imbalance normalized by the measured dijet yields, in order to study the changes in the shape of the  $x_J$  distribution as a function of the heavy-ion collision centrality. Past studies did not address the absolute rate at which dijets are produced in Pb+Pb collisions, which could assess whether leading dijets are suppressed at levels similar to those for “inclusive jets” (all jets in the event which meet  $p_T$  and rapidity selections) [3]. This paper thus presents both types of measurements with leading dijets in Pb+Pb and  $pp$  collisions at  $\sqrt{s_{NN}} = 5.02$  TeV. These measurements use  $2.2 \text{ nb}^{-1}$  of Pb+Pb collisions collected in 2015 and 2018 as well as  $260 \text{ pb}^{-1}$  of  $pp$  data collected in 2017 with the ATLAS detector [14] at the LHC.

Jets are reconstructed using the anti- $k_t$  algorithm [15] with radius parameter  $R = 0.4$ . Leading dijets are constructed from the two highest- $p_T$  jets in the event and are required to have the two jets nearly back-to-back in azimuth with  $\Delta\phi \equiv |\phi_1 - \phi_2| \geq 7\pi/8$  and  $|y| < 2.1$ .<sup>2</sup> The measurement is performed in

<sup>2</sup> ATLAS uses a right-handed coordinate system with its origin at the nominal interaction point (IP) in the center of the detector, and the  $z$ -axis along the beam pipe. The  $x$ -axis points from the IP to the center of the LHC ring, and the  $y$ -axis points upward. Cylindrical coordinates  $(r, \phi)$  are used in the transverse plane,  $\phi$  being the azimuthal angle around the  $z$ -axis. The pseudorapidity is defined in terms of the polar angle  $\theta$  as  $\eta = -\ln \tan(\theta/2)$ . The rapidity is defined as  $y = 0.5 \ln[(E + p_z)/(E - p_z)]$  where  $E$  and  $p_z$  are the energy and  $z$ -component of the momentum along the beam direction, respectively. Transverse momentum and transverse energy are defined as  $p_T = p \sin \theta$  and  $E_T = E \sin \theta$ , respectively. The angular distance between two objects with relative differences  $\Delta\eta$  in pseudorapidity and  $\Delta\phi$  in azimuth is given by  $\Delta R = \sqrt{(\Delta\eta)^2 + (\Delta\phi)^2}$ .

logarithmic  $p_T$  bins from 100 to 562 GeV for leading jets and above 32 GeV for subleading jets. Events whose two highest- $p_T$  jets do not meet the selection criteria are discarded.

The primary observable for this measurement is the two-dimensional yield of leading dijets ( $N_{\text{pair}}$ ) meeting the selection criteria:

$$\frac{d^2 N_{\text{pair}}}{dp_{T,1} dp_{T,2}}. \quad (3)$$

Projections of the two-dimensional distribution in Exp. (3) can be used to construct  $x_J$  distributions as a function of  $p_{T,1}$  and  $p_{T,2}$ . The  $x_J$  values, as defined in Eq. (2), are reported for  $0.32 < x_J < 1.0$  for selections in  $p_{T,1}$ . The minimum  $x_J$  value is chosen to be consistent with previous measurements [11]. The  $x_J$  distributions are presented with two normalizations. The first uses the dijet yield normalization to extract the *dijet-yield-normalized*  $x_J$  distributions:

$$\frac{1}{N_{\text{pair}}} \frac{dN_{\text{pair}}}{dx_J}. \quad (4)$$

This normalization, Exp. (4), has been used in previous dijet measurements by ATLAS and CMS [11–13]. The second normalization provides *absolutely normalized*  $x_J$  distributions:

$$\frac{1}{\langle T_{AA} \rangle N_{\text{evt}}^{\text{AA}}} \frac{dN_{\text{pair}}^{\text{AA}}}{dx_J} \quad (5)$$

in Pb+Pb collisions and

$$\frac{1}{L_{pp}} \frac{dN_{\text{pair}}^{pp}}{dx_J} \quad (6)$$

in  $pp$  collisions. Here  $\langle T_{AA} \rangle$  [2] is the mean nuclear thickness function for the events under consideration,  $N_{\text{evt}}^{\text{AA}}$  is the number of minimum-bias events, and  $L_{pp}$  is the integrated luminosity of the  $pp$  collisions [16]. The absolutely normalized  $x_J$  distributions allow a direct comparison between the dijet rates measured in Pb+Pb and  $pp$  collisions. Additionally, the absolutely normalized  $x_J$  distributions can be integrated over the measurement range of  $0.32 < x_J < 1.0$  to construct the pair nuclear modification factors for dijets as a function of the leading and subleading jet  $p_T$ . These quantities are defined analogously to the nuclear modification factor for inclusive jets, Eq. (1), as

$$R_{\text{AA}}^{\text{pair}}(p_{T,1}) = \frac{\frac{1}{\langle T_{AA} \rangle N_{\text{evt}}^{\text{AA}}} \int_{0.32 \times p_{T,1}}^{p_{T,1}} \frac{d^2 N_{\text{pair}}^{\text{AA}}}{dp_{T,1} dp_{T,2}} dp_{T,2}}{\frac{1}{L_{pp}} \int_{0.32 \times p_{T,1}}^{p_{T,1}} \frac{d^2 N_{\text{pair}}^{pp}}{dp_{T,1} dp_{T,2}} dp_{T,2}} \quad (7)$$

and

$$R_{\text{AA}}^{\text{pair}}(p_{T,2}) = \frac{\frac{1}{\langle T_{AA} \rangle N_{\text{evt}}^{\text{AA}}} \int_{p_{T,2}}^{p_{T,2}/0.32} \frac{d^2 N_{\text{pair}}^{\text{AA}}}{dp_{T,1} dp_{T,2}} dp_{T,1}}{\frac{1}{L_{pp}} \int_{p_{T,2}}^{p_{T,2}/0.32} \frac{d^2 N_{\text{pair}}^{pp}}{dp_{T,1} dp_{T,2}} dp_{T,1}}. \quad (8)$$

By integrating over  $p_{T,2}$  ( $p_{T,1}$ ), one can access information from  $R_{\text{AA}}^{\text{pair}}(p_{T,1})$  ( $R_{\text{AA}}^{\text{pair}}(p_{T,2})$ ) about the differential rate of dijet production in leading (subleading) jet  $p_T$  bins. Comparison of these two quantities at a fixed jet  $p_T$  provides information about the relative suppression of leading and subleading jets.

## 2 ATLAS detector

The ATLAS detector [14] at the LHC covers nearly the full solid angle around the nominal interaction point. It contains an inner tracking detector surrounded by a thin superconducting solenoid, electromagnetic and hadronic calorimeters, a zero-degree calorimeter, and a muon spectrometer which incorporates three large superconducting toroidal magnets. The inner-detector system is immersed in a 2 T axial magnetic field and provides charged-particle tracking within  $|\eta| < 2.5$ .

The ATLAS calorimeter system covers the pseudorapidity range  $|\eta| < 4.9$ . Within the region  $|\eta| < 3.2$ , electromagnetic calorimetry is provided by barrel and endcap high-granularity lead/liquid-argon (LAr) calorimeters, with an additional thin LAr presampler covering  $|\eta| < 1.8$  to allow corrections for energy lost in material upstream of the calorimeters. Hadronic calorimetry is provided by a steel/scintillator-tile calorimeter which is segmented into three barrel structures within  $|\eta| < 1.7$ , as well as two copper/LAr hadronic endcap calorimeters. To complete the solid angle coverage, forward copper/LAr and tungsten/LAr calorimeter modules (FCal) are used, optimized for electromagnetic and hadronic measurements respectively.

The zero-degree calorimeters (ZDCs) are located symmetrically at  $z = \pm 140$  m and cover  $|\eta| > 8.3$ . They are constructed using tungsten absorber plates with quartz fibers to transmit the Cherenkov light. In Pb+Pb collisions the ZDCs primarily observe “spectator” neutrons, which do not interact during the primary collision.

A two-level trigger system is used within ATLAS to select events of interest [17]. The first-level trigger is implemented in hardware and uses a subset of the detector information to reduce the event rate to at most 100 kHz. This is followed by the software-based high-level trigger, which further reduces the event rate to several kHz of triggered events that are recorded to permanent storage.

An extensive software suite [18] is used in the reconstruction and analysis of real and simulated data, in detector operations, and in the trigger and data acquisition systems of the experiment.

## 3 Data and Monte Carlo selection

The Pb+Pb data used to perform these measurements were collected in 2015 and 2018, and the  $pp$  data used were collected in 2017 with the average number of inelastic interactions per bunch crossing ranging from 1.4 to 4.4. The events were triggered using a series of various  $p_T$ -threshold single-jet triggers with the leading jets in the analysis being in a region where the trigger is fully efficient. Although only a small fraction of the Pb+Pb events ( $< 0.5\%$ ) contain multiple collisions, these were suppressed utilizing the observed anti-correlation, expected from the nuclear geometry, between the total transverse energy deposited in both of the forward calorimeters,  $\Sigma E_T^{\text{FCal}}$ , and the energy in the ZDC, which is proportional to the number of observed spectator neutrons. Pileup collisions are not rejected in  $pp$  collisions.

The overlap area of the two colliding nuclei in Pb+Pb collisions is characterized by the event centrality, which is estimated from the total transverse energy deposited in the FCal [19]. This measurement considers five centrality intervals as defined according to successive percentiles of the  $\Sigma E_T^{\text{FCal}}$  distribution obtained from minimum-bias collisions. The centrality intervals considered in this measurement are 0–10% (largest  $\Sigma E_T^{\text{FCal}}$ ), 10–20%, 20–40%, 40–60%, and 60–80% (smallest  $\Sigma E_T^{\text{FCal}}$ ). The values of the mean nuclear thickness function,  $\langle T_{AA} \rangle$  [2], are determined using the TGLAUBERMC v3.2 [20]; the uncertainties in  $\langle T_{AA} \rangle$

are discussed in Ref. [21]. The  $\langle T_{AA} \rangle$  values and their uncertainties are listed in Table 1 for each centrality selection considered in this measurement.

Table 1: The  $\langle T_{AA} \rangle$  values and uncertainties for the centrality selections used in this measurement. These are the results from TGLAUBERMC v3.2 modeling of the summed transverse energy in the forward calorimeters,  $\Sigma E_T^{\text{FCal}}$ .

Centrality selection	$\langle T_{AA} \rangle \pm \delta \langle T_{AA} \rangle$ [1/mb]
0–10%	$23.35 \pm 0.20$
10–20%	$14.33 \pm 0.17$
20–40%	$6.79 \pm 0.16$
40–60%	$1.96 \pm 0.09$
60–80%	$0.39 \pm 0.03$

This analysis uses four Monte Carlo (MC) samples to evaluate the detector performance and correct for detector effects. The  $pp$  MC sample used in this analysis includes  $3.2 \times 10^7$  PYTHIA 8 [22]  $pp$  jet events generated at  $\sqrt{s} = 5.02$  TeV with parameter values set according to the A14 tune [23] and the NNPDF23LO parton distribution functions (PDFs) [24]. Pileup due to additional  $pp$  collisions is similarly generated using PYTHIA 8 with the same PDFs and utilizing the A3 tune [25], matching the number of extra collisions in the  $pp$  data. The MC samples for Pb+Pb collisions, one for the 2015 detector conditions and one for the 2018 detector conditions, each use  $3.2 \times 10^7$   $pp$  PYTHIA 8 events with the same parameter tune and PDFs as used for the  $pp$  MC samples. The underlying event contribution to the detector signal is accounted for by overlaying the simulated  $pp$  events with dedicated Pb+Pb data events from the 2015 Pb+Pb run and 2018 Pb+Pb run respectively. The data events from Pb+Pb collisions were combined with the signal from the PYTHIA 8 simulation of hard scattering events at the digitization stage, and then reconstructed as a combined event. This procedure enables the “data overlay” sample to accurately reproduce the effects of the underlying event on the jet response. This sample was reweighted on an event-by-event basis to ensure the same centrality distribution as is measured in the jet-triggered data samples. The detector response in all three MC samples was simulated utilizing GEANT4 [26, 27]. Finally,  $pp$  Herwig++ [28] events using the UEEE5 tune [29] and the CTEQ6L1 PDFs [30] are used for uncertainty studies.

## 4 Jet reconstruction and performance

The jet reconstruction procedures follow those used by ATLAS for previous jet measurements in Pb+Pb collisions [3, 9]. Jets are reconstructed using the anti- $k_t$  algorithm [15] implemented in the FastJet software package [31]. In both  $pp$  and Pb+Pb collisions, jets with  $R = 0.2$  and  $R = 0.4$  are formed by clustering calorimetric towers of spatial size  $\Delta\eta \times \Delta\phi = 0.1 \times \pi/32$ . The energies in the towers are obtained by summing the energies of calorimeter cells at the electromagnetic energy scale [32] within the tower boundaries. In Pb+Pb collisions, a background subtraction procedure is applied to estimate, within each event, the underlying event (UE) average transverse energy density,  $\rho(\eta, \phi)$ , where the  $\phi$  dependence is due to global azimuthal correlations in the particle production from the hydrodynamic flow [33]. The modulation accounts for the contribution to the UE of the second-, third-, and fourth-order azimuthal anisotropy harmonics characterized by values of flow coefficients  $v_n^{\text{UE}}$  [33]. Additionally, the UE is also corrected for  $\eta$ - and  $\phi$ -dependent nonuniformities of the detector response by correction factors derived in minimum-bias Pb+Pb data. In  $pp$  collisions, the same background subtraction procedure is applied to remove the pileup contribution to the jet, but without the  $\phi$ -dependent modulation and without the correction for  $\eta$ - and  $\phi$ -dependent nonuniformities.

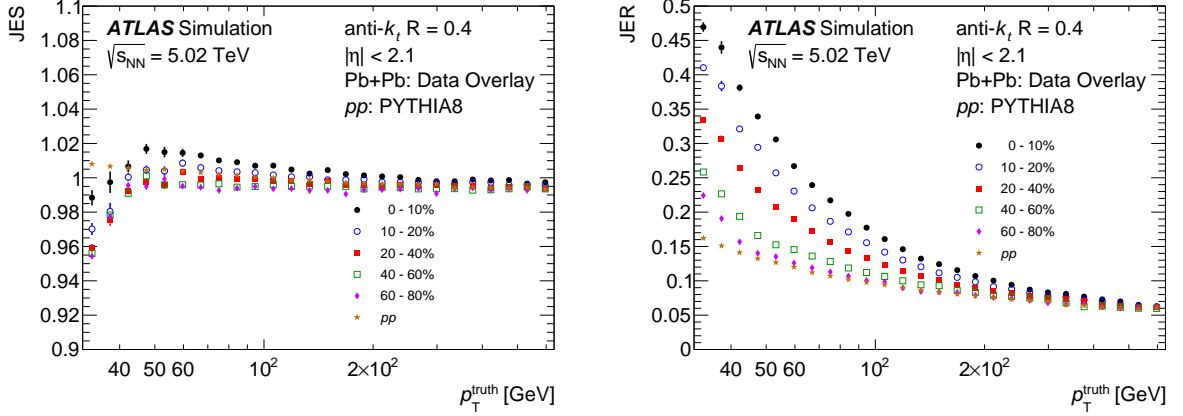


Figure 1: The jet energy scale, JES, (left) and jet energy resolution, JER, (right) as a function of  $p_T^{\text{truth}}$  for centrality selections in Pb+Pb and in  $pp$  collisions.

An iterative procedure is used to remove the impact of jets on the estimated  $\rho$  and  $v_n^{\text{UE}}$  values. The first estimate of the average transverse energy density of the UE,  $\rho(\eta)$ , is evaluated in 0.1 intervals of  $\eta$ , excluding towers within  $\Delta R = 0.4$  of “seed” jets. In the first subtraction step, the seeds are defined to be a combination of  $R = 0.2$  jets and  $R = 0.4$  track-jets. Track-jets are reconstructed by applying the anti- $k_t$  algorithm with  $R = 0.4$  to charged particles with  $p_T > 4$  GeV. The  $R = 0.2$  jets must pass a cut on the minimum value of the tower  $E_T$  and on a ratio of maximum tower  $E_T$  to average tower  $E_T$ , while the track-jets are required to have  $p_T > 7$  GeV. The underlying event contribution is then subtracted from each tower constituent and the jet kinematics are recalculated. After the first iteration, the  $\rho$  and  $v_n$  values are updated by excluding from the UE determination the regions within  $\Delta R = 0.4$  of both the track-jets and the newly reconstructed  $R = 0.2$  jets with  $p_T > 25$  GeV (8 GeV) in Pb+Pb ( $pp$ ) collisions. The updated  $\rho$  and  $v_n^{\text{UE}}$  values are used to update the jet kinematic properties in the second iteration. Jet  $\eta$ - and  $p_T$ -dependent correction factors derived in simulations are applied to the measured jet energy to correct for the calorimeter energy response [34, 35]. An additional correction based on in situ studies of jets recoiling against photons and jets in other regions of the calorimeter is applied [36]. This calibration is followed by a “cross-calibration” which relates the jet energy scale (JES) of jets reconstructed by the procedure outlined in this section to the JES in 13 TeV  $pp$  collisions [35].

“Truth”-level jets are defined in the MC sample before detector simulation by applying the anti- $k_t$  algorithm with  $R = 0.4$  to stable particles with a proper lifetime greater than 30 ps, but excluding muons and neutrinos, which do not leave significant energy deposits in the calorimeter. After the detector simulation the truth jets are matched to the nearest reconstructed jet within  $\Delta R < 0.3$ . The performance of the jet reconstruction is characterized by the JES and jet energy resolution (JER), which correspond to the mean and variance of the  $p_T^{\text{reco}}/p_T^{\text{truth}}$  distribution, where  $p_T^{\text{reco}}$  is the reconstructed jet  $p_T$  and  $p_T^{\text{truth}}$  is the  $p_T$  of the matched truth-level jet. The JES and JER as a function of  $p_T^{\text{truth}}$  can be seen in Figure 1. The decrease in the JES for jets with  $p_T^{\text{truth}} < 50$  GeV in Pb+Pb collisions stems from jets for which there is an over subtraction of the underlying event. This is caused by the corresponding region of the detector not containing a “seed” jet above 25 GeV resulting in the jets energy contributing to the UE determination; this is corrected for in the unfolding procedure discussed below. The efficiency of reconstructing a jet with  $p_T > 32$  GeV, as evaluated from the probability of a truth-jet matching to a reconstructed jet with  $p_T > 32$  GeV in the MC simulation, can be seen as a function of  $p_T^{\text{truth}}$  in Figure 2.



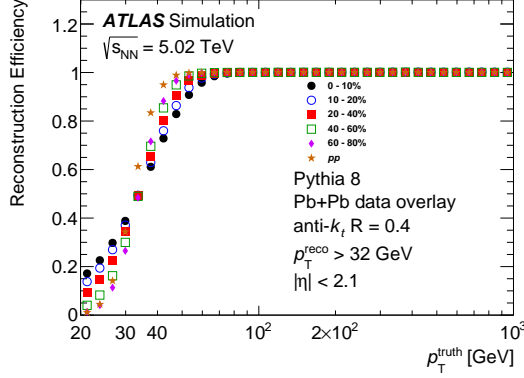


Figure 2: The efficiency of reconstructing a jet with  $p_T^{\text{reco}} > 32$  GeV as a function of  $p_T^{\text{truth}}$  for centrality selections in Pb+Pb collisions and  $pp$  collisions. The statistical uncertainties shown are smaller than the point markers.

## 5 Data analysis

The analysis and dijet selection used here closely follow those in Ref. [11]. In each data event, the reconstructed leading dijet is constructed from the two highest- $p_T^{\text{reco}}$  jets in the event with reconstructed  $p_{T,1}^{\text{reco}} > 79$  GeV and  $p_{T,2}^{\text{reco}} > 32$  GeV, and both jets are required to have  $|y| < 2.1$ . The inclusion of leading jets down to  $p_{T,1}^{\text{reco}} > 79$  GeV provides an underflow region for the unfolding to enable inflow and outflow of jets from the measurement region. These dijets are required to be back-to-back with  $|\Delta\phi| > 7\pi/8$ . Events in which the leading dijets do not meet these criteria are discarded. For dijets matching the selection criteria, two-dimensional  $(p_{T,1}^{\text{reco}}, p_{T,2}^{\text{reco}})$  distributions are constructed symmetrically across  $p_{T,1}^{\text{reco}} = p_{T,2}^{\text{reco}}$ . The distributions are symmetrized to account for the possibility of swapping the leading and subleading jet definition due to the finite JER.

The analysis procedure selects at most one dijet per event and therefore has the potential to produce a biased subsample of the inclusive jets. Figure 3 shows the fraction of the inclusive jets which are also included in the leading dijets used in this analysis. This quantity is shown as a function of  $p_T^{\text{reco}}$  for both central Pb+Pb and  $pp$  collisions. The fraction is 83% (85%) at 100 GeV and rises to more than 95% (95%) at 200 GeV in central Pb+Pb collisions ( $pp$  collisions). Due to the steep falloff of the jet yields with increasing  $p_T$  and the finite JER, jets reconstructed at a given  $p_T$  typically arise from jets at a lower truth  $p_T$ , and thus the fractions shown here at the reconstructed- $p_T$  scale underestimate the true fraction of inclusive jets included at a given  $p_T$ . Nevertheless, the large value, and weak  $p_T$  dependence, of the fraction of inclusive jets that are part of the leading dijet imply that the dijet selection in this analysis does not produce a particularly biased sample. The fractions are further broken down by leading and subleading jets.

The measured  $(p_{T,1}^{\text{reco}}, p_{T,2}^{\text{reco}})$  distributions are a combination of the dijet signal and pairs of uncorrelated jets. Since the underlying-event subtraction accounts for azimuthal correlations in the particle production due to hydrodynamic flow, the contribution from uncorrelated dijets is independent of the  $\Delta\phi$  of the jets; therefore, a  $\Delta\phi$  sideband method is used to remove these pairs as a function of  $(p_{T,1}^{\text{reco}}, p_{T,2}^{\text{reco}})$ . The symmetrized two-dimensional  $(p_{T,1}^{\text{reco}}, p_{T,2}^{\text{reco}})$  distribution of background combinatoric dijets is determined using dijets with  $1 < |\Delta\phi| < 1.4$  which, after normalizing to the  $\Delta\phi$  window of the signal band, is subtracted from the dijet yields. This effect is strongest for 0–10% centrality Pb+Pb events at low  $p_{T,1}^{\text{reco}}$ , where combinatoric dijets constitute 13% of the dijets for  $79 < p_{T,1}^{\text{reco}} < 100$  GeV, and drops off rapidly both with increasing  $p_{T,1}^{\text{reco}}$  and in more peripheral events. Because of how the leading dijet is defined, the



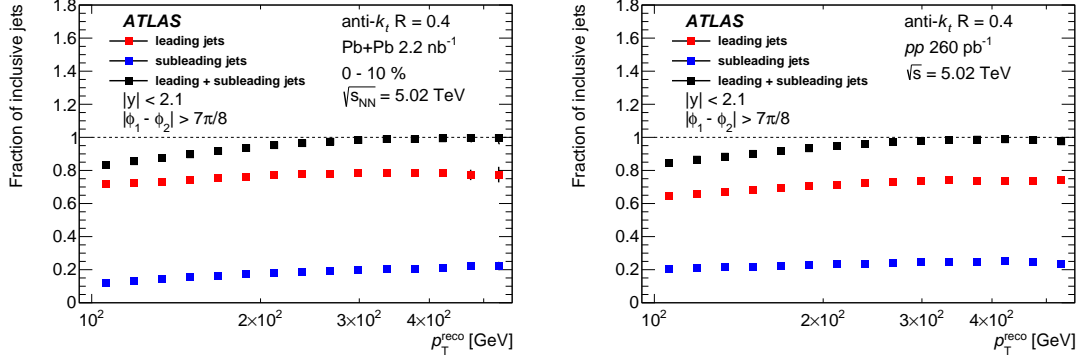


Figure 3: Measured fractions of the inclusive jets which are part of the leading dijet (black), the leading jet of the dijet (red), or subleading jet of the dijet (blue), all as a function of  $p_T^{\text{reco}}$  for 0–10% centrality Pb+Pb collisions (left) and  $pp$  collisions (right).

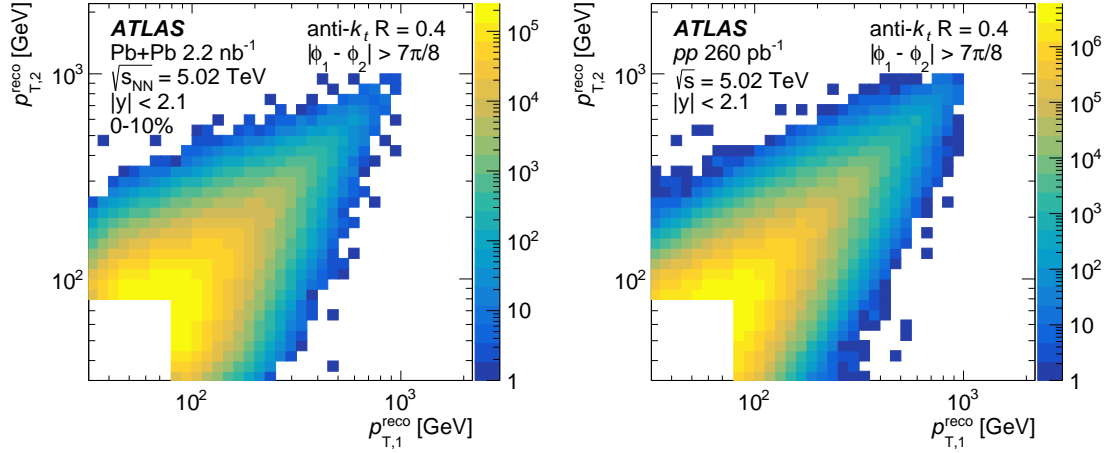


Figure 4: The background-subtracted and symmetrized  $(p_{T,1}^{\text{reco}}, p_{T,2}^{\text{reco}})$  distributions, measured in data, in 0–10% centrality Pb+Pb collisions (left) and  $pp$  collisions (right).

presence of residual combinatoric dijets in the sample results in an inefficiency for genuine jet pairs, where one of the jets might be superseded by an uncorrelated third jet. This effect is corrected for using the measured inclusive jet spectrum from minimum-bias events to determine the efficiency loss as a function of the measured jet  $p_T$  following the method discussed in Ref. [11]. The resulting combinatoric-subtracted and efficiency-corrected symmetrized two-dimensional  $(p_{T,1}^{\text{reco}}, p_{T,2}^{\text{reco}})$  distributions can be seen in Figure 4 for both central Pb+Pb and  $pp$  collisions. The ability to remove uncorrelated jets and extract the truth-level leading-dijet  $x_J$  distributions in an unbiased way was confirmed by a closure test performed using the data overlay sample.

In order to correct for the effects of the JES and JER, the measured  $(p_{T,1}^{\text{reco}}, p_{T,2}^{\text{reco}})$  distributions are unfolded using the iterative Bayesian unfolding procedure [37] as implemented in the RooUnfold [38] software package. A two-dimensional unfolding is used in order to account for bin migrations of both the leading and the subleading jet  $p_T$ , as well as to account for possible swapping of the leading and subleading jet. A separate response matrix is generated for  $pp$  collisions as well as for each centrality selection in Pb+Pb

collisions. The response matrix used in the unfolding contains the relationship between  $(p_{T,1}^{\text{truth}}, p_{T,2}^{\text{truth}})$  and  $(p_{T,1}^{\text{reco}}, p_{T,2}^{\text{reco}})$ . It is populated by identifying the leading and subleading truth-level jets in the MC sample which are matched to the corresponding reconstructed jets within  $\Delta R < 0.3$ . In order to account for migration from lower jet  $p_T^{\text{reco}}$ , the response matrices are populated with truth-level jets down to  $p_{T,1}^{\text{truth}}$  of 20 GeV and  $p_{T,2}^{\text{truth}}$  of 10 GeV. As with the reconstructed data, truth dijets are required to have  $|\Delta\phi_{\text{truth}}| > 7\pi/8$ , with each jet being within  $|y_{\text{truth}}| < 2.1$ . The two selected reconstructed jets from the MC simulations are required to meet the same selection criteria as applied to dijets measured in data. Truth dijets that do not match to a reconstructed dijet meeting the selection criteria are accounted for by using an efficiency correction in the unfolding. Similarly to the construction of the data distributions, the response matrix is populated symmetrically in  $p_{T,1}$  and  $p_{T,2}$ . To construct a Bayesian prior which is similar to the measured distributions, the response matrices are reweighted along the  $p_{T,1}^{\text{truth}}$  and  $p_{T,2}^{\text{truth}}$  axes by the ratio of the two-dimensional reconstructed yields in data to those from simulation. The number of iterations used in the unfolding is tuned separately for each centrality in Pb+Pb collisions and for  $pp$  collisions. The number of iterations in each case was selected to optimize the balance between the accuracy of the final unfolded yield, and the increased statistical uncertainty which results from a larger number of iterations. Six iterations were used for the 0–10% centrality Pb+Pb events, while four iterations were used for all other centralities as well as for  $pp$  collisions.

In order to evaluate the statistical uncertainties of the data and the MC simulation, 1000 unfoldings were performed by varying each bin in either the data distribution or the response matrix independently according to its statistical uncertainty while preserving the symmetrization across  $p_{T,1} = p_{T,2}$ . The RMS of the resulting unfolded distributions in each  $(p_{T,1}, p_{T,2})$  bin was taken as the contribution to the statistical uncertainty on the corresponding unfolded  $(p_{T,1}, p_{T,2})$  bin. The data and response matrix statistical uncertainty components were combined in quadrature in order to obtain the total statistical uncertainty of the unfolded distributions. Due to the large number of bins in the two-dimensional unfolding, in some cases the uncertainties due to the finite MC sample sizes are comparable to those in the data.

To extract measurements of the dijet momentum balance observable,  $x_J$ , the unfolded two-dimensional  $(p_{T,1}, p_{T,2})$  distributions are first reflected about  $p_{T,1} = p_{T,2}$  in order to restore the leading/subleading hierarchy. Then, following the procedure discussed in Ref. [11], the two-dimensional distributions are projected in slices of  $p_{T,1}$  into bins of  $x_J$ . The  $x_J$  bin boundaries are defined by  $((p_{T,N}/p_{T,0})^{1/N})^{i-N}$ , where  $N$  is the number of logarithmic  $p_T$  bins (40), and  $p_{T,0}$  and  $p_{T,N}$  are the minimum (10 GeV) and maximum (1 TeV) bin edges covered by the binning, respectively. This enables the mapping of the logarithmic  $p_{T,1}$  and  $p_{T,2}$  bins to  $x_J$  in such a way that each reported  $(p_{T,1}, p_{T,2})$  bin is fully contained within two adjacent  $x_J$  bins. In this analysis, half of the yield in each  $(p_{T,1}, p_{T,2})$  bin is apportioned to each of the two adjacent  $x_J$  bins. An exception to this are the bins along the diagonal  $p_{T,1} = p_{T,2}$ , which contribute solely to the highest  $x_J$  bin.

By projecting the resulting distributions over selections of  $p_{T,1}$  while normalizing by the number of dijets ( $N_{\text{pair}}$ ) and accounting for the  $x_J$  bin widths, measurements of the dijet yield-normalized  $x_J$  distributions are extracted. The absolutely-normalized  $x_J$  distributions are extracted by instead normalizing the  $x_J$  distributions by the number of events and either the  $T_{AA}$  in Pb+Pb collisions or the integrated luminosity in  $pp$  collisions, as described by Exp. (5).

In order to quantify the energy losses of the leading and subleading jets within a dijet, the nuclear modification factor,  $R_{AA}^{\text{pair}}$ , is measured for each of these selections. The  $R_{AA}^{\text{pair}}$  compares the per-event differential yield of jets at a given  $p_T$  in Pb+Pb collisions with the cross-section in  $pp$  collisions scaled by the  $T_{AA}$ , as described in Eqs. (7) and (8).

## 6 Systematic uncertainties

Systematic uncertainties for this measurement are attributed to three categories of sources, those which arise from the analysis and unfolding procedure, those which stem from uncertainties in the jet energy resolution (JER) and scale (JES), and those connected with global normalization. For each uncertainty component in the first two categories, the entire analysis procedure, including unfolding, is repeated accounting for the modification to the analysis procedure or the response matrix and the result is compared with the nominal one. The third category applies to the absolutely-normalized  $x_J$  distributions,  $R_{AA}^{\text{pair}}(p_{T,1})$ , and  $R_{AA}^{\text{pair}}(p_{T,2})$ ; it contains the uncertainty in the determination of the mean nuclear thickness function,  $\langle T_{AA} \rangle$ , and the  $pp$  luminosity. These uncertainties are independent of the jet transverse momentum and are noted on the figures.

The systematic uncertainty in the JES has four parts. First, a centrality-independent baseline component is determined from in situ studies of the calorimeter response to jets reconstructed with the procedure used in 13 TeV  $pp$  collisions [39]. A second, centrality-independent component accounts for the relative energy scale difference between the jet reconstruction procedures used in this analysis and those in 13 TeV  $pp$  collisions. This is evaluated using the cross-calibration procedure described in Ref. [35]. Potential inaccuracies in the PYTHIA 8 MC sample's description of the relative abundances of jets initiated by quarks and gluons and of the calorimetric response to quark and gluon jets are accounted for by the third, centrality independent, component – based on evaluating these same quantities using the Herwig++ MC sample. The fourth, centrality-dependent, component accounts for modifications of the parton shower due to quenching [40], which is not modeled in the simulations. The modifications to the parton shower can impact the detector response to jets in Pb+Pb collisions resulting in a small disagreement in the JES between data and simulations. The extent of this disagreement, and corresponding uncertainty contribution is evaluated by the method used in Ref. [35] for 2015 and 2011 data, which compares the jet  $p_T$  measured in the calorimeter with the sum of the transverse momenta of charged particles within the jet, in both the data and MC samples. This uncertainty is determined as a function of event centrality and was found to be independent of jet  $p_T$  and  $\eta$ . The selected charged-particle tracks have  $p_T > 4$  GeV in order to exclude particles from the UE. The sum of the charged-particle transverse momenta provides a data-driven estimate of the centrality dependence of the JES arising from the observed centrality-dependent modification of the jet fragmentation due to jet quenching in Pb+Pb collisions [40]. The size of this centrality-dependent uncertainty in the JES reaches 1.2% in the most central collisions and the value is applied independent of  $x_J$ . For each individual component, the JES in the MC simulation was modified as a function of  $p_T$  and  $\eta$  by one standard deviation, and the response matrix was recomputed.

The uncertainty due to the JER is evaluated by repeating the unfolding procedure with modified response matrices, where an additional contribution is added to the resolution of the reconstructed  $p_T$  in the MC sample using a Gaussian smearing procedure. The smearing factor is evaluated using an in situ technique in 13 TeV  $pp$  data that involves studies of dijet  $p_T$  balance [41]. Further, an uncertainty is included to account for differences between the tower-based jet reconstruction and the jet reconstruction used in analyses of 13 TeV  $pp$  data, as well as differences in calibration procedures. The modifications to the response are propagated through the unfolding and the resulting uncertainty is symmetrized.

Two sources of systematic uncertainty were included to account for uncertainties in the removal of the combinatoric background. The first contribution stems from the combinatoric subtraction method, and was determined by extracting the two-dimensional  $(p_{T,1}, p_{T,2})$  distribution of combinatoric jets from an alternative sideband of  $1.1 < |\Delta\phi| < 1.5$  as was done in Ref. [11]. The second contribution stems from the

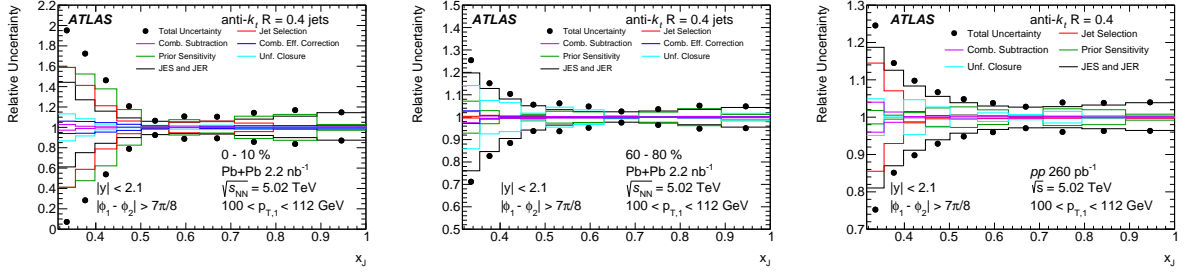


Figure 5: The systematic uncertainty breakdown of the  $x_J$  distributions in central (left) and peripheral (center) Pb+Pb collisions as well as  $pp$  collisions (right). The panels have different vertical axis ranges.

sensitivity of the analysis to the efficiency correction for combinatoric jets, and was evaluated by repeating the analysis without the inclusion of this efficiency correction. The deviation from the nominal result is taken as the uncertainty contribution.

Additional sources of systematic uncertainty which account for the unfolding procedure were considered. The sensitivity to the Bayesian prior was evaluated by modifying the weights applied when producing the response matrix in a centrality-dependent manner in order to enclose the data ( $p_{T,1}^{\text{reco}}, p_{T,2}^{\text{reco}}$ ) distributions between the corresponding MC distributions based on the nominal and alternative priors. There is a sensitivity to the minimum  $p_T^{\text{jet}}$  in the analysis at small  $x_J$  and small  $p_{T,1}$  due to the efficiency correction made as part of the unfolding. The sensitivity of the result to this effect is evaluated by varying the minimum reconstructed  $p_T^{\text{jet}}$ , motivated by the magnitude of the JER, from 32 to 39 GeV for both data and simulation. This results in a significant contribution to the systematic uncertainties at low  $x_J$  in low  $p_{T,1}$  bins. For each of these contributions the deviation of the unfolded result from the nominal is symmetrized and taken as a contribution to the systematic uncertainties. A closure test was performed using the MC samples by splitting them into two equal parts and using one part to produce a response matrix and the other in place of the data sample in the unfolding. The deviation between the unfolded result and the underlying truth-level distribution was taken as an estimate of this uncertainty. The uncertainty from each of these contributions is taken independently and symmetrized.

The magnitude of the systematic uncertainties in the dijet-yield-normalized  $x_J$  distributions can be seen in Figure 5 for both central and peripheral Pb+Pb collisions. In the central collisions, the total systematic uncertainties are largely driven by the sensitivity of the unfolding to the choice of prior. In contrast, in peripheral collisions the total uncertainties are largely driven by the uncertainty in the JES and JER. The fractional uncertainties are largest at low  $x_J$  in both collision systems; however, the yield in these  $x_J$  regions is small.

The systematic uncertainty contributions are similarly propagated to the calculation of the nuclear modification factor. The centrality-independent components of the JES and JER, as well as the sensitivity of the unfolding to the minimum measured  $p_T^{\text{jet}}$ , are treated as correlated between Pb+Pb and  $pp$ . The remainder of the contributions to the systematic uncertainty, including the centrality-dependent component of the JES, are treated as uncorrelated between Pb+Pb and  $pp$ . The resulting uncertainties in  $R_{AA}^{\text{pair}}(p_{T,1})$  and  $R_{AA}^{\text{pair}}(p_{T,2})$  are shown for 0–10% centrality Pb+Pb collisions in Figure 6; these uncertainties are dominated by the JES uncertainty. In the ratio of  $R_{AA}^{\text{pair}}(p_{T,2})$  to  $R_{AA}^{\text{pair}}(p_{T,1})$ , each source of systematic uncertainty is treated as fully correlated between  $R_{AA}^{\text{pair}}(p_{T,2})$  and  $R_{AA}^{\text{pair}}(p_{T,1})$ , including the global systematic uncertainties.

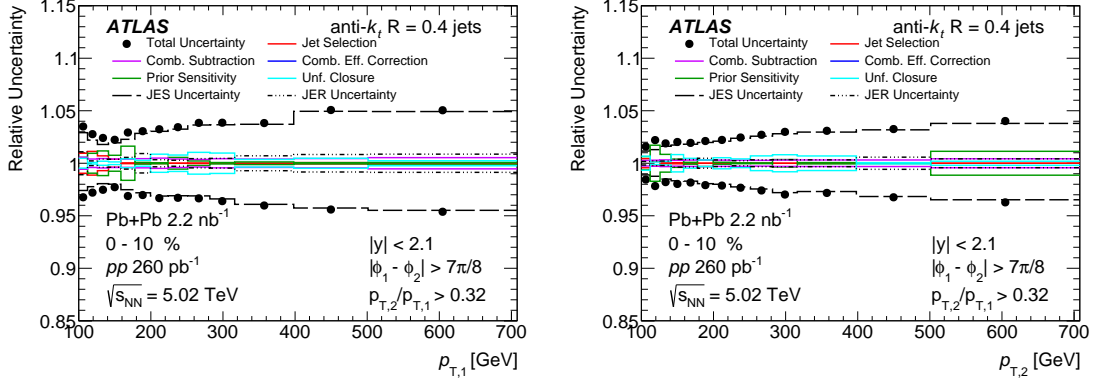


Figure 6: The systematic uncertainty breakdown of the  $R_{AA}^{\text{pair}}$  for leading jets (left) and subleading jets (right). Uncertainty on the  $T_{AA}$  and  $pp$  luminosity are not shown.

## 7 Results

### 7.1 Dijet-yield-normalized $x_J$ distributions

The dijet-yield-normalized  $x_J$  distributions in  $pp$  collisions are shown for three selections of  $p_{T,1}$  from 100 to 562 GeV in Figure 7. The measured distributions are compared with those from the PYTHIA 8 generator [22] using the A14 tune [23] in combination with the NNPDF23<sub>LO</sub> PDFs [24]. The PYTHIA 8 sample is able to describe the data over the full  $x_J$  range considered.

Figure 8 shows the measured dijet-yield-normalized  $x_J$  distributions in  $pp$  collisions and as a function of centrality in Pb+Pb collisions for twelve  $p_{T,1}$  selections between 100 and 562 GeV. In central collisions, at  $100 < p_{T,1} < 112$  GeV a broad maximum is observed in the distributions at  $x_J$  around 0.6. With increasing  $p_{T,1}$  as well as with decreasing centrality, this feature becomes less pronounced. Significant modification from  $pp$  collisions is observed up to  $398 < p_{T,1} < 562$  GeV in the full centrality range; the  $x_J$  distributions have a reduced fraction of balanced jets and an increased fraction of imbalanced jets.

Figure 9 compares the measured distributions in Pb+Pb collisions with the predictions from the LIDO model [42]. LIDO is a transport model including both elastic jet-medium collisions and medium-induced radiative processes, as well as a simple model for the response of the medium. LIDO uses PYTHIA 8 [22] with the A14 tune [23] and the CTEQ1.1 PDF [30] to initialize their energy-loss calculation. The calculations are performed using two values for the jet-medium coupling cutoff parameter:  $\mu_{\text{min}} = 1.3$  and  $\mu_{\text{min}} = 1.8$ . This parameter is related to the strength of the coupling between the jet and the medium, where a smaller  $\mu_{\text{min}}$  value corresponds to a larger coupling, and was constrained using inclusive jet and hadron suppression measurements [42]. Only minimal sensitivity to the jet-medium coupling cutoff parameter is observed in the dijet-yield-normalized  $x_J$  distributions, with  $\mu_{\text{min}} = 1.3$  and  $\mu_{\text{min}} = 1.8$  demonstrating equal ability to reproduce the measured results. The model reproduces the behavior observed at high  $p_{T,1}$  and in 40–60% centrality Pb+Pb collisions while not reproducing the relative enhancement of intermediate  $x_J$  observed at low  $p_{T,1}$  in 0–10% centrality Pb+Pb collisions.

Figure 10 shows a direct comparison between the dijet-yield-normalized  $x_J$  distributions in 0–10% centrality Pb+Pb collisions at 5.02 TeV for  $100 < p_{T,1} < 200$  GeV and results at 2.76 TeV from Ref. [11] for the same collision centrality and  $p_{T,1}$  selections. Although these two measurements are performed at different

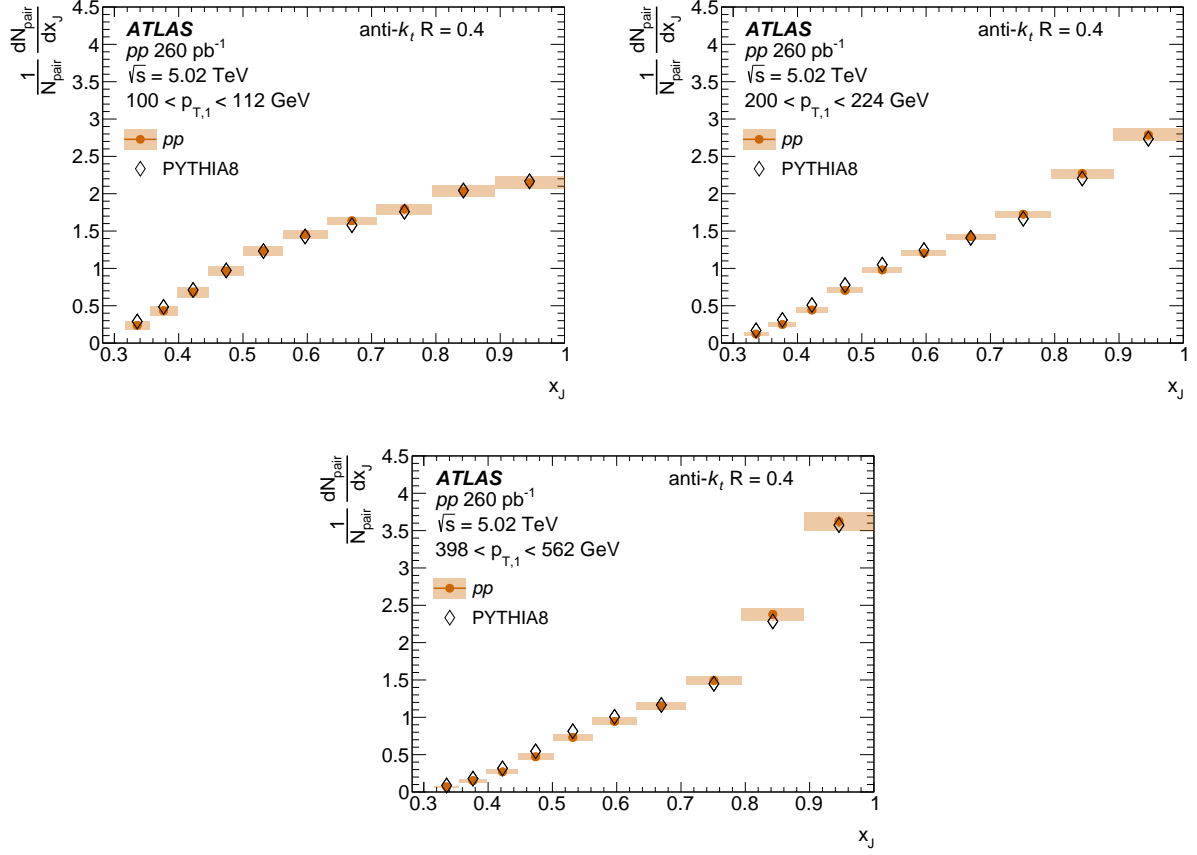


Figure 7: The dijet-yield-normalized  $\frac{1}{N_{\text{pair}}} \frac{dN_{\text{pair}}}{dx_J}$  distributions in  $pp$  collisions for three  $p_{T,1}$  selections from 100 GeV to 562 GeV overlaid with the corresponding distributions from PYTHIA 8. The statistical uncertainties are shown as error bars (which are smaller than the markers in many cases), and the systematic uncertainties are shown as boxes.

collision energies, similar levels of quenching are expected, based measurements of inclusive jets [3, 43]. The  $x_J$  distributions are observed to be consistent within systematic uncertainties at the two collision energies. For  $100 < p_{T,1} < 126$  GeV, a peak is observed at intermediate  $x_J$  for both collision energies.

## 7.2 Absolutely normalized $x_J$ distributions

The absolutely normalized  $x_J$  distributions, as calculated with Exps. (5) and (6) for Pb+Pb and  $pp$  collisions respectively, allow a direct comparison of the absolute dijet yields between Pb+Pb and  $pp$  collisions as a function of  $x_J$ . Figure 11 shows these distributions for  $pp$  and Pb+Pb collisions as a function of centrality for three  $p_{T,1}$  selections: 100–112 GeV, 200–224 GeV, and 398–562 GeV. Balanced dijets are suppressed in central Pb+Pb collisions relative to asymmetric dijets, leading to the peak structure observed in the dijet-yield-normalized  $x_J$  distributions at low  $p_{T,1}$ . The depletion of balanced dijets persists over all  $p_{T,1}$  and centrality selections measured here, with the magnitude of the depletion decreasing with increasing  $p_{T,1}$  and towards more peripheral collisions. When going from central Pb+Pb collisions to  $pp$  collisions for  $100 < p_{T,1} < 112$  GeV, the suppression of dijets is smaller for  $x_J < 0.6$  than for higher  $x_J$ . For higher  $p_{T,1}$ , there is a smaller difference between  $pp$  and Pb+Pb collisions at low  $x_J$ .

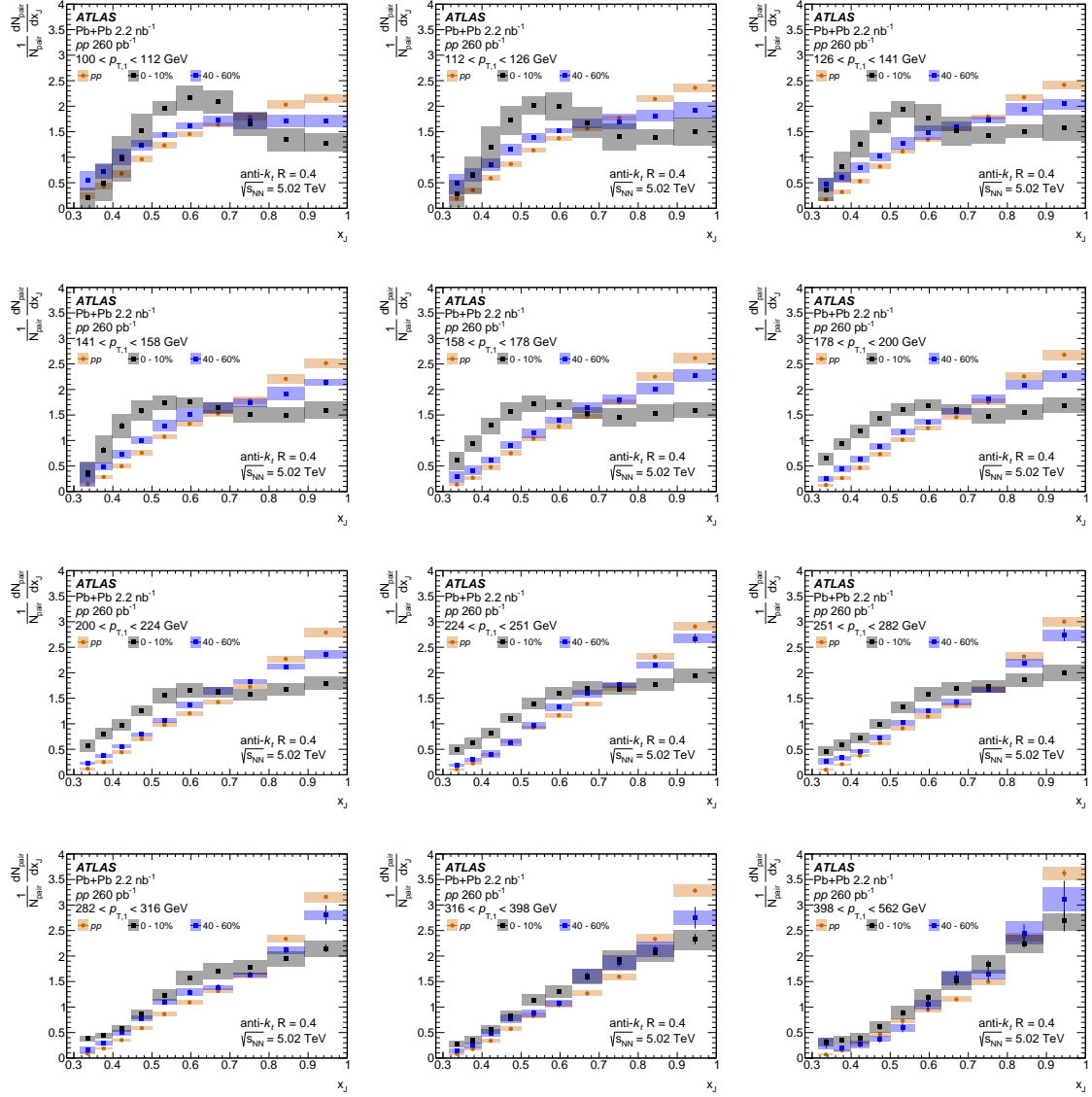


Figure 8: The dijet-yield-normalized  $\frac{1}{N_{\text{pair}}} \frac{dN_{\text{pair}}}{dx_j}$  distributions in 0–10% and 40–60% centrality Pb+Pb collisions and  $pp$  collisions for twelve  $p_{T,1}$  selections from 100 GeV to 562 GeV. Statistical uncertainties are shown as error bars (which are smaller than the markers in many cases) and systematic uncertainties are shown as boxes.

Figure 12 shows the absolutely normalized  $x_j$  distributions compared with the same LIDO calculations [42] as in the previous section for three  $p_{T,1}$  selections from 100 to 562 GeV. The LIDO  $pp$  calculation is also shown. For  $pp$  collisions, LIDO uses PYTHIA 8 [22] with the A14 tune [23] and the CTEQ1 PDF [30]. The LIDO model overestimates the  $pp$  collision results at large  $x_j$ ; the size of the discrepancy between the model and the data decreases with increasing  $p_{T,1}$ . This trend persists, but with a smaller difference in 40–60% centrality Pb+Pb collisions. In 0–10% centrality Pb+Pb collisions, the LIDO model’s prediction is flatter than the data in the lowest  $p_{T,1}$  range, but agrees well at higher  $p_{T,1}$ .



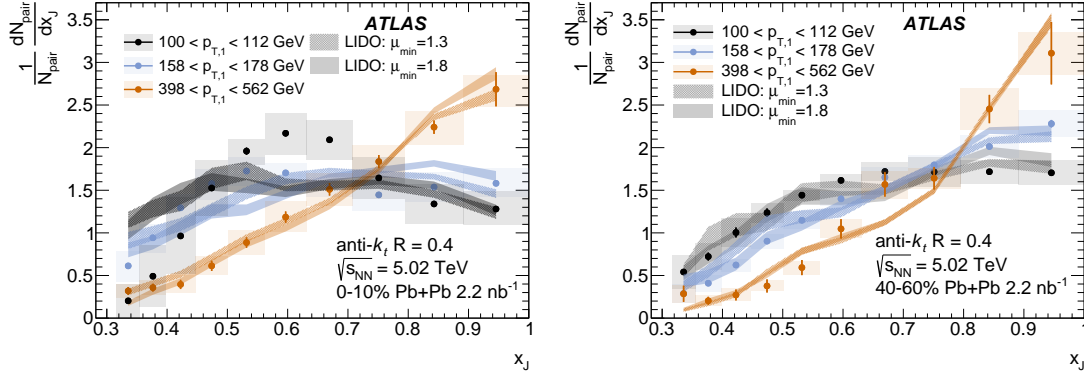


Figure 9: Comparison of the dijet-yield-normalized  $x_J$  distributions in 0–10% (left) and 40–60% (right) centrality Pb+Pb collisions with predictions from LIDO [42] for two values of the jet–medium coupling cutoff parameter,  $\mu_{\min} = 1.3$ , and  $\mu_{\min} = 1.8$ . Statistical uncertainties are shown as error bars (which are smaller than the markers in many cases) and systematic uncertainties are shown as boxes.

### 7.3 $R_{AA}^{\text{pair}}$ of leading and subleading jets

The pair nuclear modification factors projected for leading and subleading jets, as defined in Eqs. (7) and (8), are shown for three centrality selections as a function of the jet  $p_T$  in Figure 13. Both  $R_{AA}^{\text{pair}}(p_{T,1})$  and  $R_{AA}^{\text{pair}}(p_{T,2})$  show significant modification from a value of one in all but the most peripheral collisions, with a stronger suppression observed at low  $p_T^{\text{jet}}$ . It is observed that the subleading jets are more suppressed than leading jets, particularly at  $p_T > 200$  GeV where nearly all the inclusive jets (within the rapidity range of this analysis) are included in the dijet sample. This behavior is qualitatively reproduced in predictions made by the LIDO [42] model. In the LIDO model, the jet–medium coupling cutoff parameter  $\mu_{\min} = 1.3$  clearly predicts a larger suppression for both jets than is observed in the data. The calculation with  $\mu_{\min} = 1.8$  is closer to the data but does not describe the trends with  $p_T$  and centrality.

The different levels of suppression observed for leading and subleading jets is quantified as a function of centrality in the ratio  $R_{AA}^{\text{pair}}(p_{T,2})/R_{AA}^{\text{pair}}(p_{T,1})$  integrated over  $p_T^{\text{jet}}$  between 100 and 316 GeV as shown in Figure 14, where  $R_{AA}^{\text{pair}}(p_{T,2})$  is seen to be smaller than  $R_{AA}^{\text{pair}}(p_{T,1})$  in all centrality selections. The suppression of subleading jets relative to leading jets is most significant in 0–10% centrality Pb+Pb collisions and decreases smoothly towards peripheral Pb+Pb collisions. In 0–10% centrality Pb+Pb events, subleading jets are approximately 20% more suppressed than leading jets, with 60–80% centrality Pb+Pb events seeing only about 5% more suppression for subleading jets than for leading jets. The value of  $R_{AA}^{\text{pair}}(p_{T,2})/R_{AA}^{\text{pair}}(p_{T,1})$  in 60–80% centrality Pb+Pb events is  $3\sigma$  away from one, providing evidence of jet quenching in peripheral Pb+Pb collisions. In contrast, in inclusive jet measurements, due to the larger uncertainties, no significant suppression is observed in this  $p_T$  range for the most peripheral Pb+Pb collisions [3]. This is in qualitative agreement with results from CMS [44], which find that, compared to  $pp$  collisions, the subleading jets in dijet events in Pb+Pb collisions have stronger modification to their structure than leading jets.

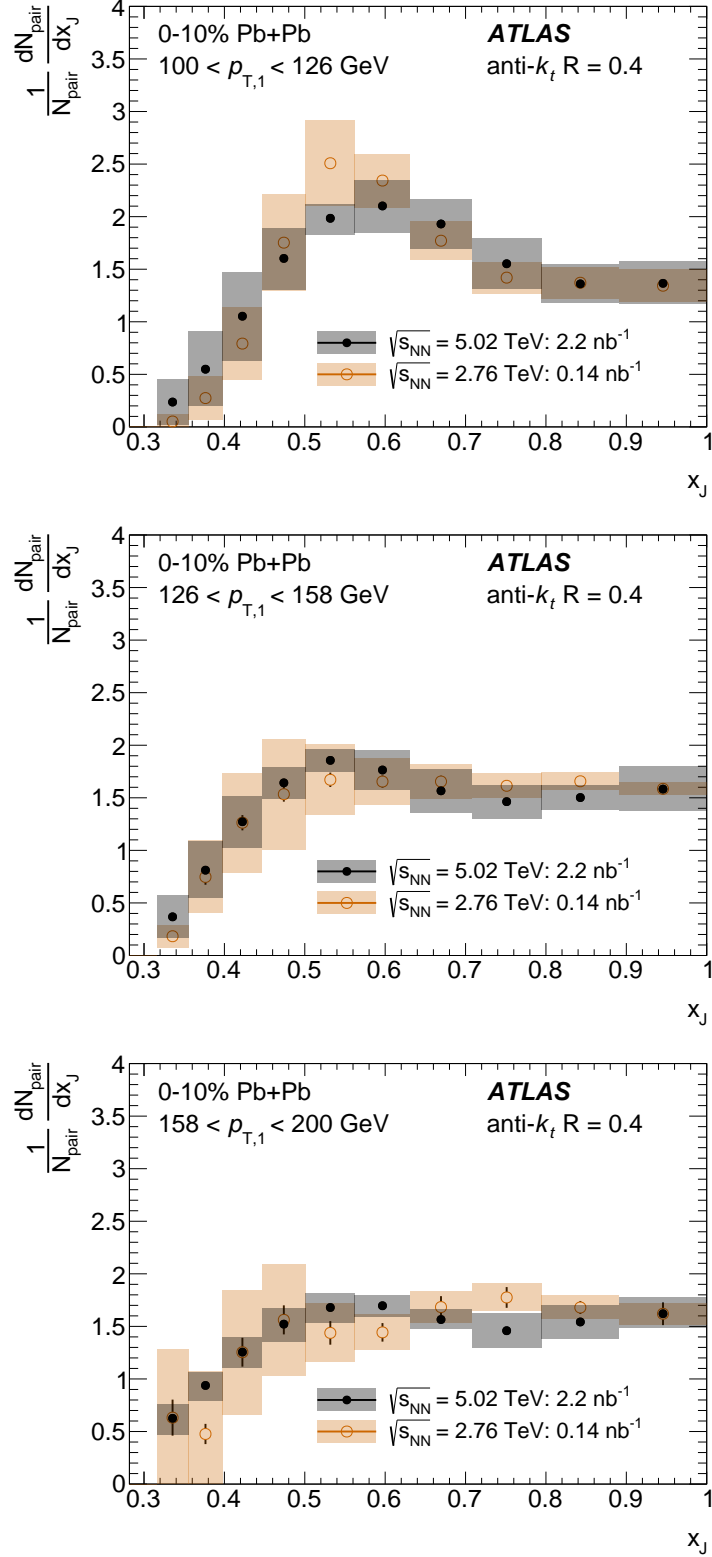


Figure 10: Comparison of the measured  $x_J$  distribution at 5.02 TeV in 0–10% centrality collisions for  $100 < p_{T,1} < 126$  GeV (top),  $126 < p_{T,1} < 158$  GeV (middle), and  $158 < p_{T,1} < 200$  GeV (bottom) with those at 2.76 TeV from Ref. [11]. Statistical uncertainties are shown as error bars (which are smaller than the markers in many cases) and systematic uncertainties are shown as boxes.

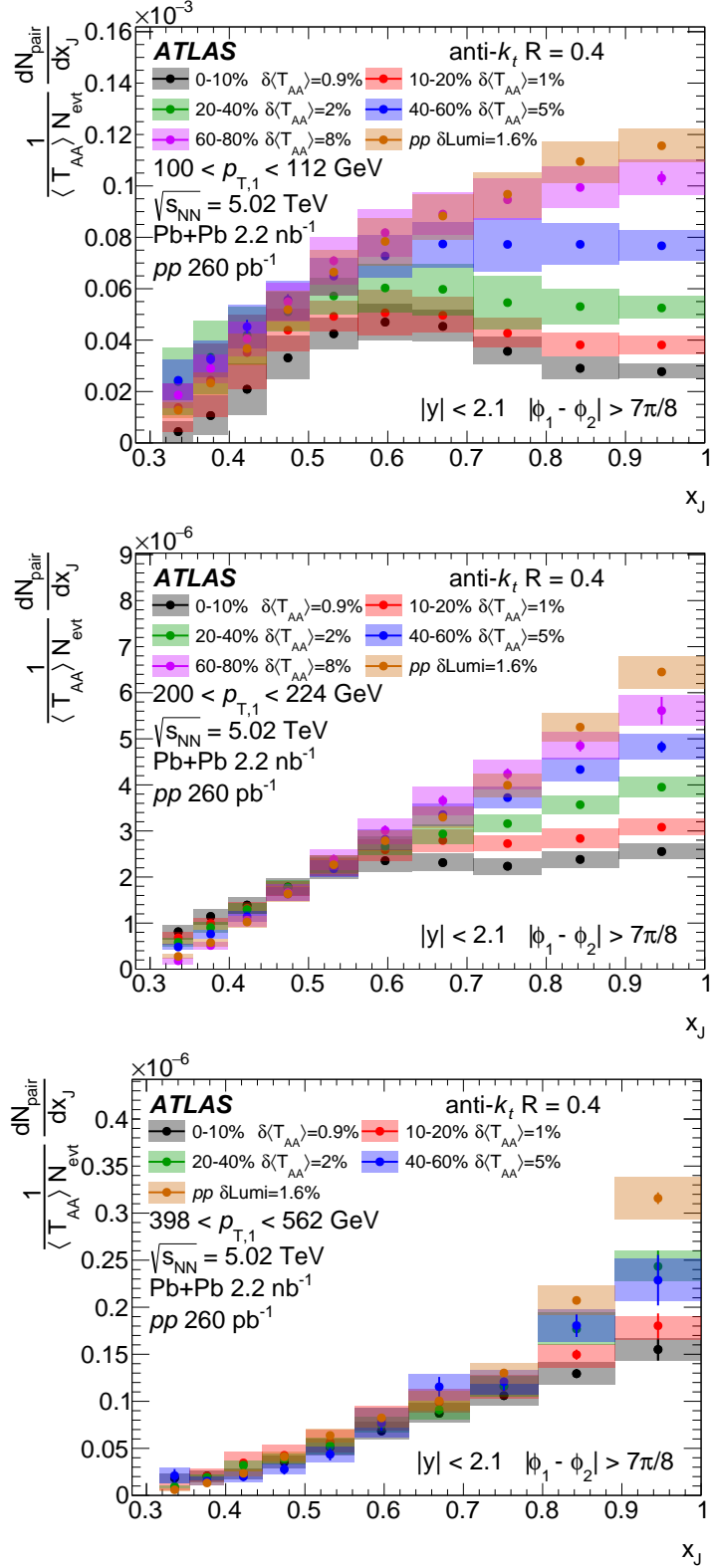


Figure 11: The absolutely normalized  $x_J$  distributions for  $100 < p_{T,1} < 112$  GeV (top),  $200 < p_{T,1} < 224$  GeV (center), and  $398 < p_{T,1} < 562$  GeV (bottom) in  $pp$  collisions and for five centrality selections in Pb+Pb collisions. Statistical uncertainties are shown as error bars (which are smaller than the markers in many cases) and systematic uncertainties are shown as boxes. The global normalization uncertainties due to the  $T_{AA}$  for each centrality as well as the  $pp$  luminosity are listed in the legends.

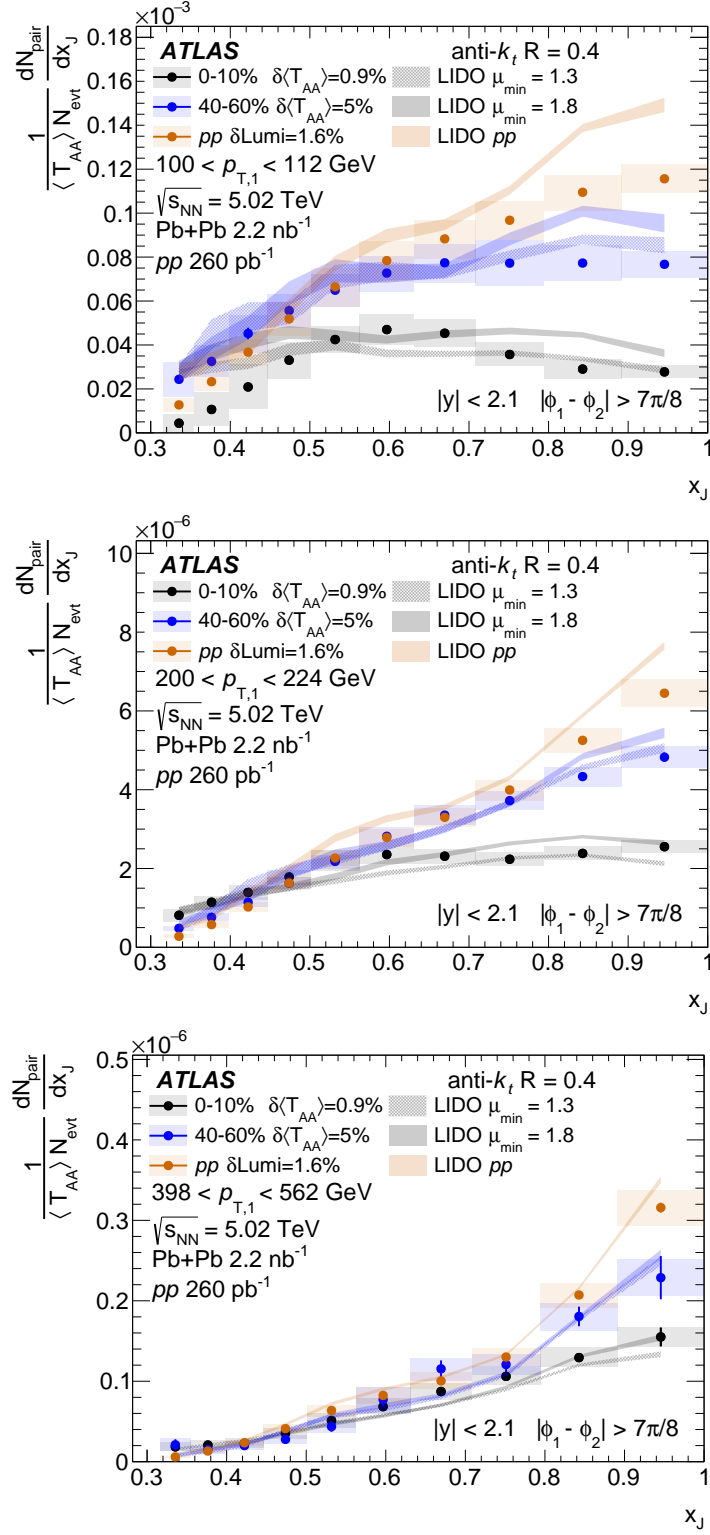


Figure 12: The absolutely normalized  $x_J$  distributions for  $100 < p_{T,1} < 112$  GeV (top),  $200 < p_{T,1} < 224$  GeV (center), and  $398 < p_{T,1} < 562$  GeV (bottom) in  $pp$  collisions and for two centrality selections in Pb+Pb collisions. For Pb+Pb collisions, the measurements are compared with predictions from LIDO [42] for two values of the jet-medium coupling cutoff parameter,  $\mu_{min} = 1.3$  and  $\mu_{min} = 1.8$ , and the  $pp$  collision measurements are compared with the LIDO  $pp$  collision calculation.

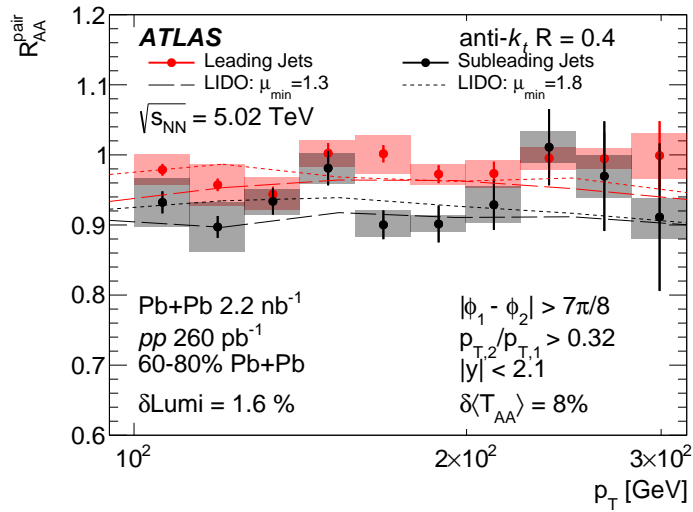
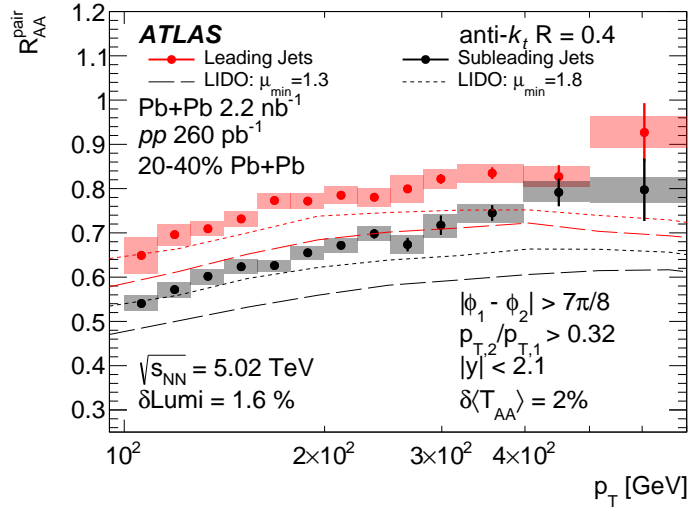
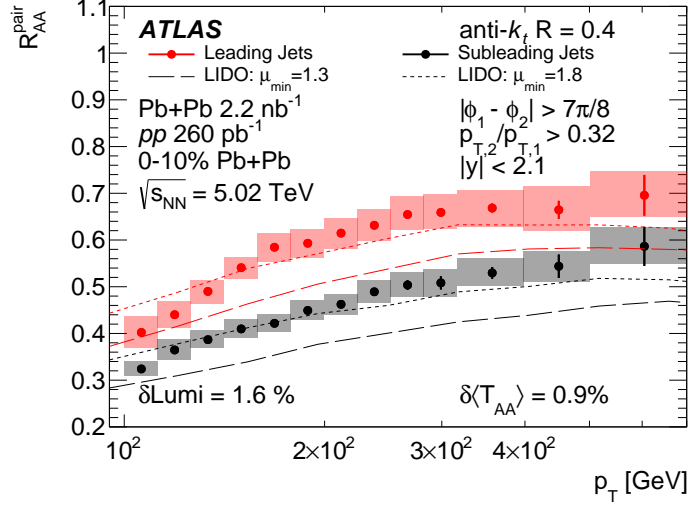


Figure 13: The leading and subleading jet  $R_{AA}^{\text{pair}}$  distributions measured for a selection of centrality regions compared with predictions from LIDO [42]. Statistical uncertainties are shown as error bars (which are smaller than the markers in many cases) and systematic uncertainties are shown as boxes.

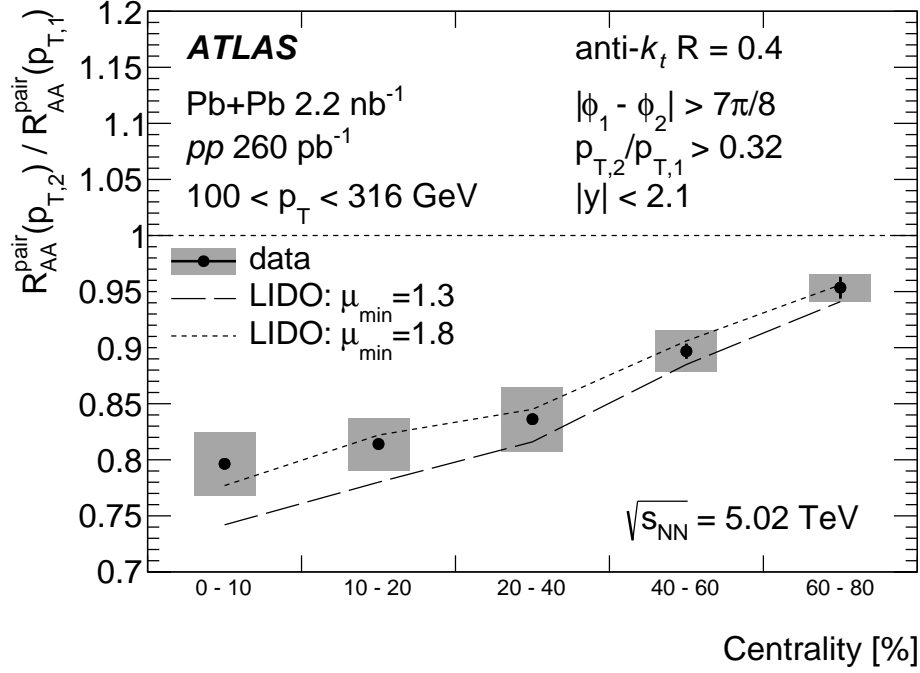


Figure 14: The ratio of the subleading-jet to leading-jet nuclear modification factors integrated over jet  $p_T$  between 100 and 316 GeV. Statistical uncertainties are shown as error bars (which are smaller than the markers in many cases) and systematic uncertainties are shown as boxes.

## 8 Conclusion

This paper presents a measurement of the unfolded double-differential yields of leading dijets. The yields are presented as measurements of the dijet  $x_J$  distributions and the  $R_{AA}^{\text{pair}}$  projected for leading and subleading jets, using 2.2 nb<sup>-1</sup> of Pb+Pb data and 260 pb<sup>-1</sup> of  $pp$  data collected at  $\sqrt{s_{NN}} = 5.02$  TeV by the ATLAS detector at the LHC. The measurement of the  $x_J$  distributions is performed differentially in  $p_{T,1}$  and centrality, and the  $R_{AA}$  of leading and subleading jets is measured differentially in jet  $p_T$  and centrality. The presented results are unfolded to correct for detector response and inefficiencies.

The dijet-yield-normalized  $x_J$  distributions, across the full  $p_{T,1}$  range considered in this analysis, show significant broadening in central Pb+Pb collisions relative to those in  $pp$  collisions. Up to the highest  $p_{T,1}$  interval considered in this measurement,  $398 < p_{T,1} < 562$  GeV, significant modification from the distributions in  $pp$  collisions is observed for central Pb+Pb collisions. With decreasing  $p_{T,1}$  the modifications from the distributions in  $pp$  collisions become larger, with significant modifications observed for all centralities at  $100 < p_{T,1} < 112$  GeV. In 0–10% centrality Pb+Pb collisions, between 100 and 112 GeV, the distribution is peaked around  $x_J$  of 0.6, indicating that the most probable configuration for dijets is to be highly imbalanced in  $p_T$ . Measurements of absolutely normalized  $x_J$  distributions show that this comes from the suppression of balanced dijets, as opposed to an enhancement of imbalanced jets, in comparison with  $pp$  collisions. This suppression of balanced dijets evolves smoothly as a function of the event centrality, with peripheral Pb+Pb collisions demonstrating only slight modification from  $pp$  collisions. The measurements of the pair nuclear modification factor,  $R_{AA}^{\text{pair}}(p_{T,1})$  and  $R_{AA}^{\text{pair}}(p_{T,2})$ , show

that subleading jets are more suppressed than leading jets. This is observed to be largely independent of jet  $p_T$  and this behavior is seen in all centralities. In central collisions, subleading jets are observed to be 20% more suppressed than the leading jets. In peripheral collisions, the suppression of subleading jets relative to leading jets is reduced, but the stronger suppression of subleading jets remains significant. These measurements provide new information about the role of path-length dependence and fluctuations in jet energy loss which will help constrain models of parton energy loss in the quark–gluon plasma.



## Appendix

For completeness, the data including the full range of  $p_{T,1}$  intervals and centrality selections in Pb+Pb collisions are included here. Figure 15 shows the dijet-yield-normalized distributions for  $pp$  collisions, compared to PYTHIA 8 calculations. Figure 16 shows unfolded  $\frac{1}{N_{\text{pair}}} \frac{dN_{\text{pair}}}{dx_J}$  distributions for both Pb+Pb and  $pp$  collisions over twelve selections in  $p_{T,1}$  between 100 and 562 GeV, for centrality intervals omitted previously. Figure 17 shows absolutely normalized  $x_J$  distributions for five centrality intervals for both Pb+Pb and  $pp$  collisions for 12 selections of  $p_{T,1}$  between 100 and 562 GeV. Finally, Figure 18 provides  $R_{\text{AA}}^{\text{pair}}(p_{T,1})$  and  $R_{\text{AA}}^{\text{pair}}(p_{T,2})$  distributions measured in two additional centrality intervals.

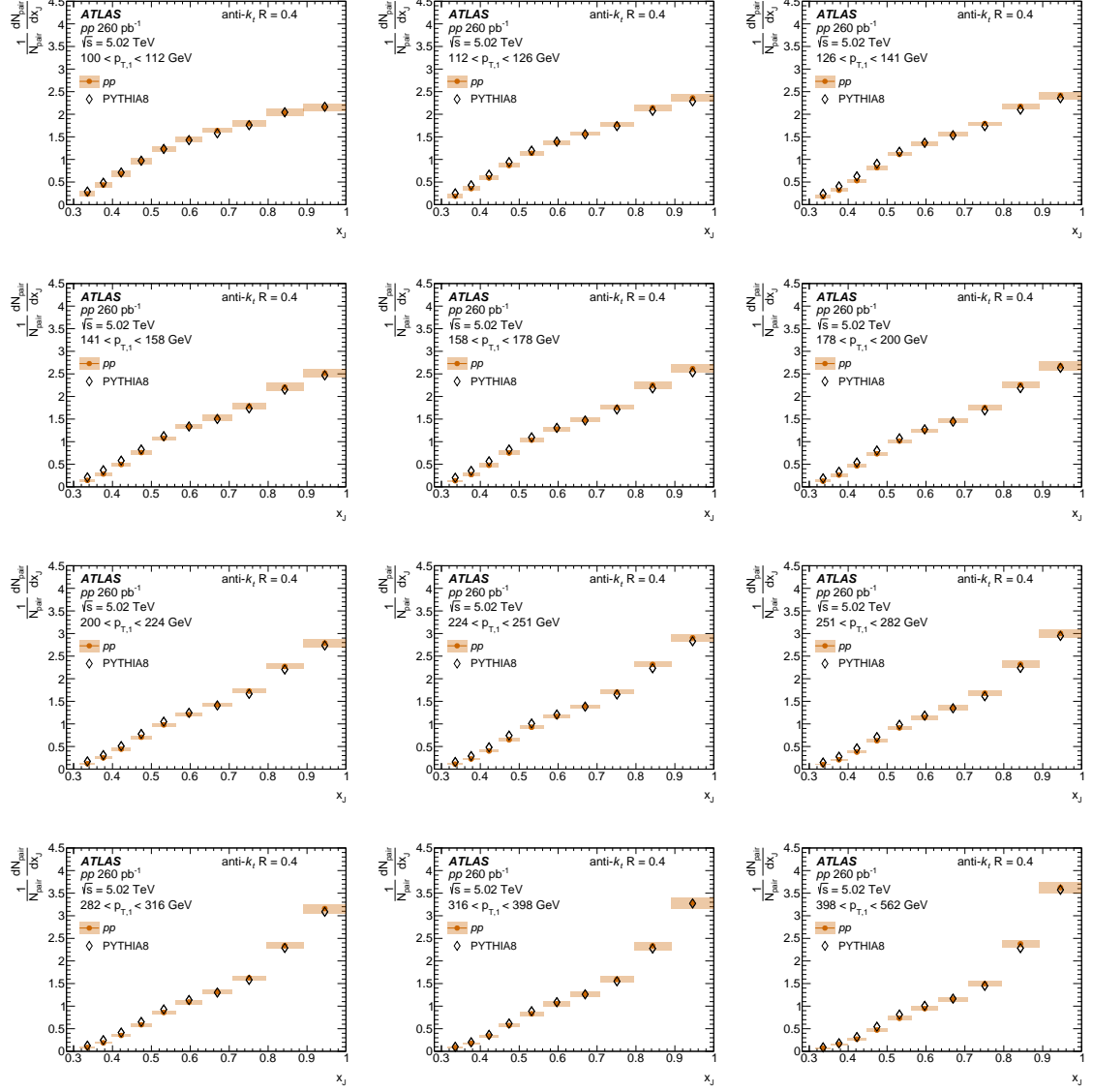


Figure 15: The dijet-yield-normalized  $\frac{1}{N_{\text{pair}}} \frac{dN_{\text{pair}}}{dx_j}$  distributions in  $pp$  collisions for twelve  $p_{T,1}$  selections from 100 GeV to 562 GeV overlaid with the corresponding distributions from PYTHIA 8. The statistical uncertainties are shown as error bars (which are smaller than the markers in many cases), and the systematic uncertainties are shown as boxes.

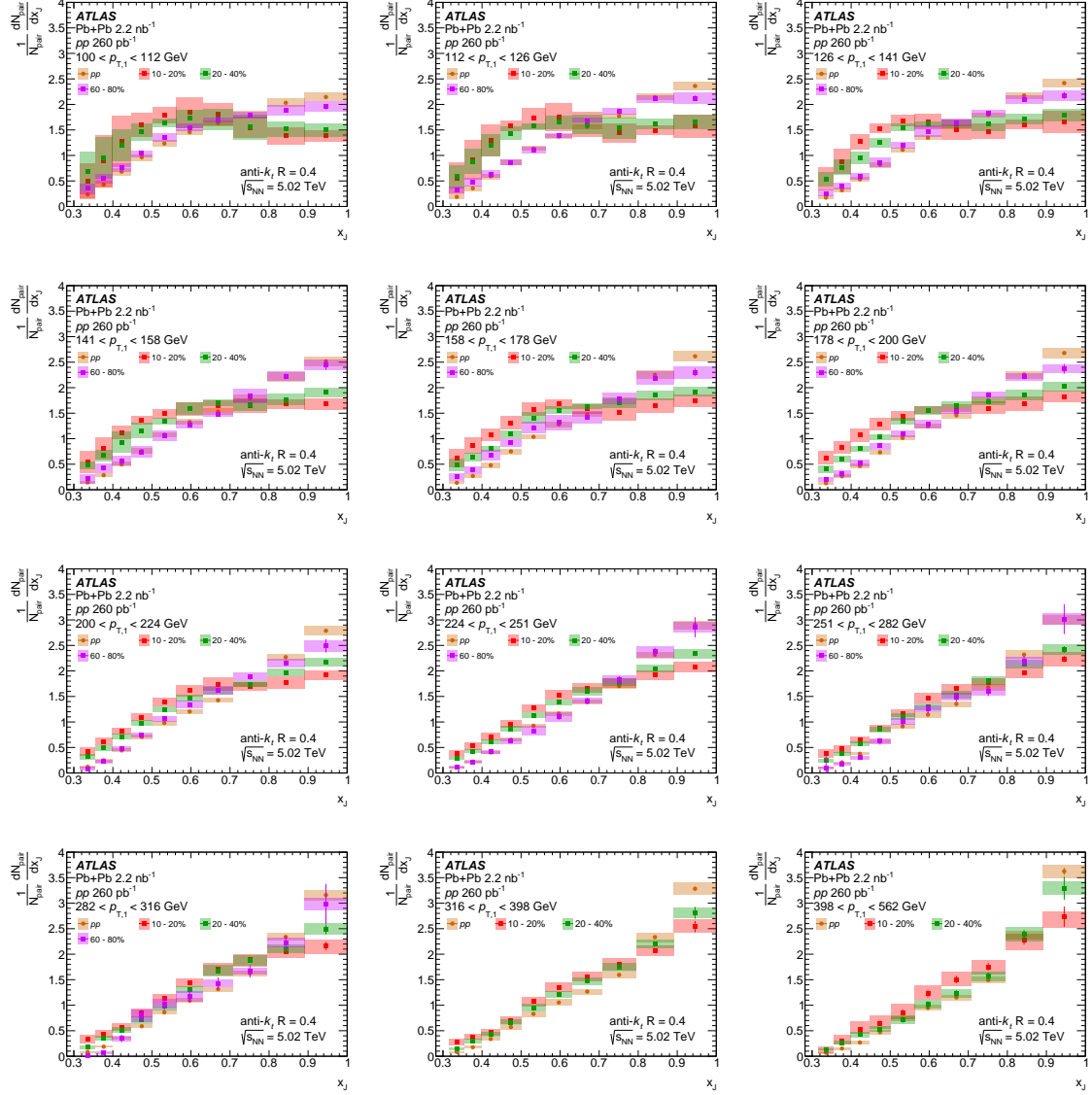


Figure 16: The unfolded dijet-yield-normalized  $x_J$  distributions in both Pb+Pb and  $pp$  collisions for twelve  $p_{T,\text{leading}}$  selections from 100 GeV to 562 GeV. The results in Pb+Pb collisions are shown in three centrality selections, 10–20%, 20–40% and 60–80%. Statistical uncertainties are shown as error bars and systematic uncertainties are shown as boxes.

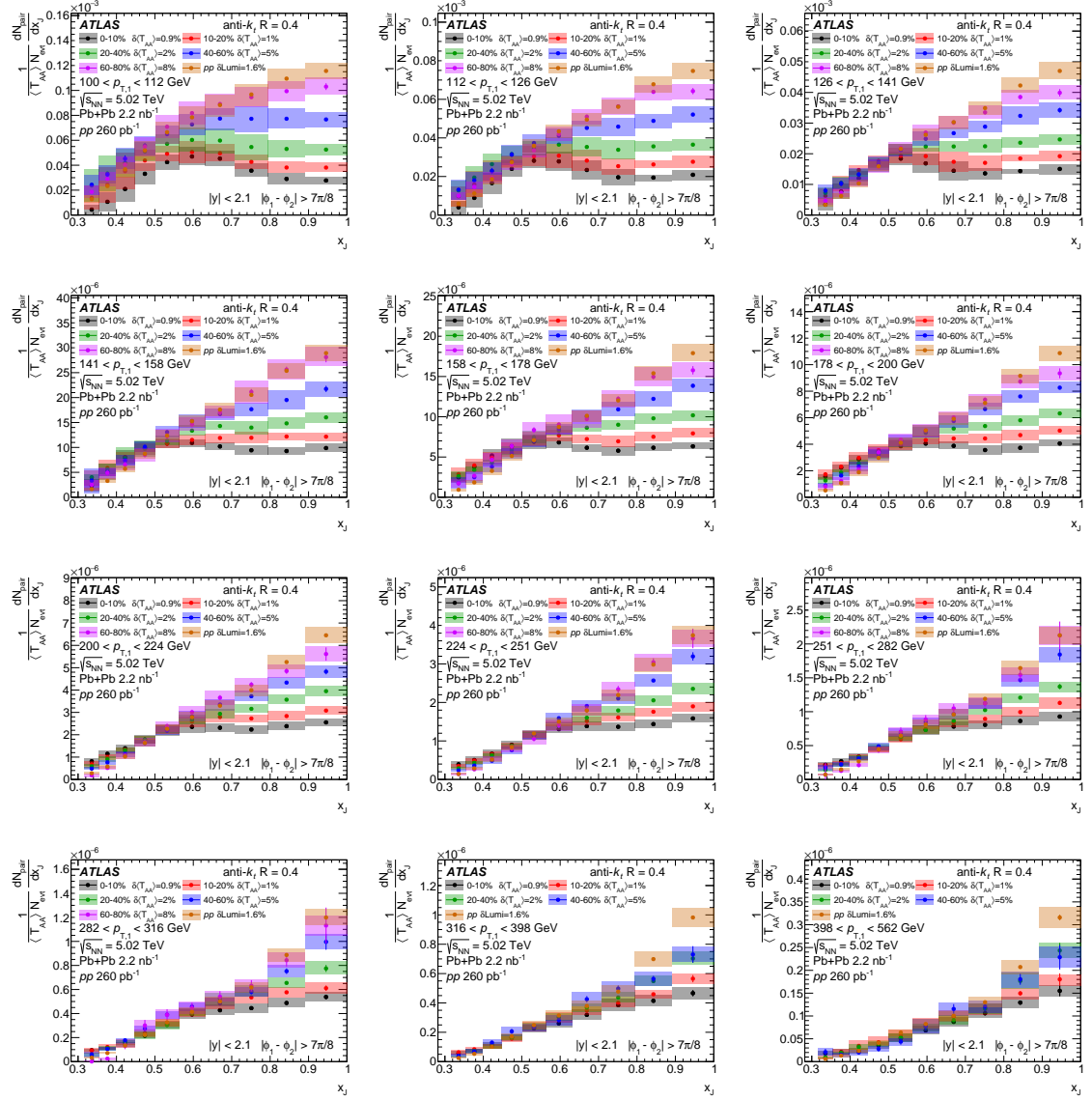


Figure 17: Comparison of the absolutely normalized  $x_J$  distributions in  $pp$  collisions and five centrality selections in Pb+Pb collisions.

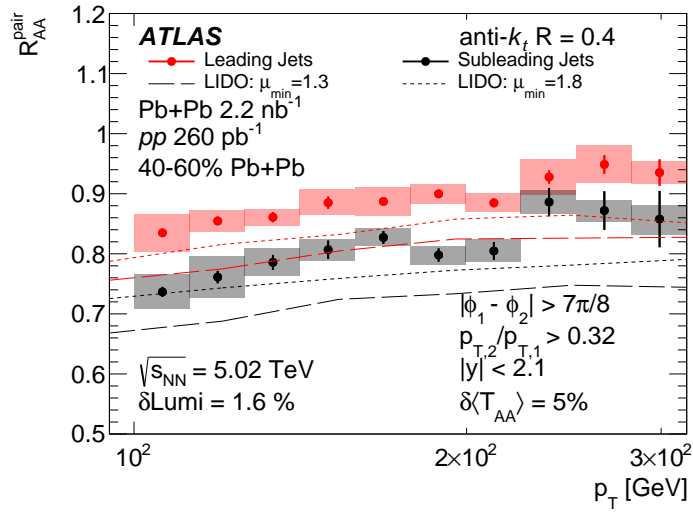
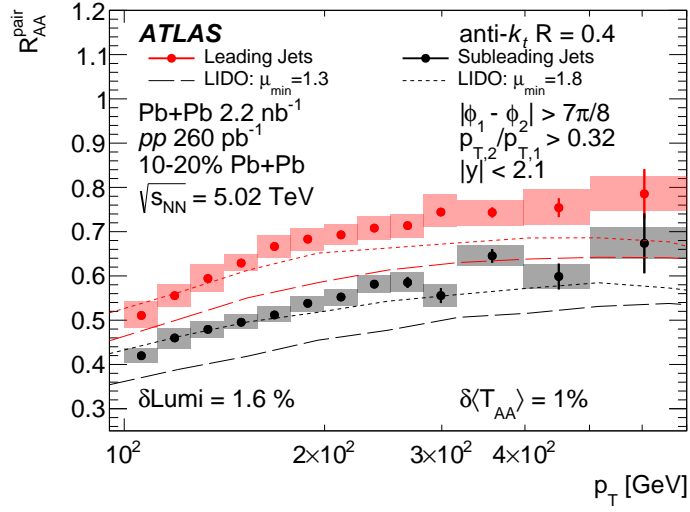


Figure 18: The  $R_{AA}^{\text{pair}}(p_{T,1})$  and  $R_{AA}^{\text{pair}}(p_{T,2})$  distributions measured for Pb+Pb centrality selections compared with predictions from LIDO [42].

## References

- [1] W. Busza, K. Rajagopal and W. van der Schee,  
*Heavy Ion Collisions: The Big Picture, and the Big Questions*,  
[Ann. Rev. Nucl. Part. Sci. \*\*68\*\* \(2018\) 339](#), arXiv: [1802.04801 \[hep-ph\]](#).
- [2] M. L. Miller, K. Reygers, S. J. Sanders and P. Steinberg,  
*Glauber modeling in high energy nuclear collisions*, [Ann. Rev. Nucl. Part. Sci. \*\*57\*\* \(2007\) 205](#),  
arXiv: [nucl-ex/0701025](#).
- [3] ATLAS Collaboration, *Measurement of the nuclear modification factor for inclusive jets in Pb+Pb collisions at  $\sqrt{s_{NN}} = 5.02$  TeV with the ATLAS detector*, [Phys. Lett. B \*\*790\*\* \(2019\) 108](#),  
arXiv: [1805.05635 \[nucl-ex\]](#).
- [4] CMS Collaboration,  
*First measurement of large area jet transverse momentum spectra in heavy-ion collisions*,  
[JHEP \*\*05\*\* \(2021\) 284](#), arXiv: [2102.13080 \[hep-ex\]](#).
- [5] ALICE Collaboration,  
*Measurements of inclusive jet spectra in pp and central Pb-Pb collisions at  $\sqrt{s_{NN}} = 5.02$  TeV*,  
[Phys. Rev. C \*\*101\*\* \(2020\) 034911](#), arXiv: [1909.09718 \[nucl-ex\]](#).
- [6] S. Cao and X.-N. Wang,  
*Jet quenching and medium response in high-energy heavy-ion collisions: a review*,  
[Rept. Prog. Phys. \*\*84\*\* \(2021\) 024301](#), arXiv: [2002.04028 \[hep-ph\]](#).
- [7] L. Cunqueiro and A. M. Sickles, *Studying the QGP with Jets at the LHC and RHIC*,  
[Prog. Part. Nucl. Phys. \*\*124\*\* \(2022\) 103940](#), arXiv: [2110.14490 \[nucl-ex\]](#).
- [8] G.-Y. Qin and B. Müller,  
*Explanation of Dijet Asymmetry in Pb+Pb Collisions at the Large Hadron Collider*,  
[Phys. Rev. Lett. \*\*106\*\* \(2011\) 162302](#), arXiv: [1012.5280 \[hep-ph\]](#),  
Erratum: [Phys. Rev. Lett. \*\*106\*\* \(2011\) 162302](#).
- [9] ATLAS Collaboration, *Measurements of azimuthal anisotropies of jet production in Pb+Pb collisions at  $\sqrt{s_{NN}} = 5.02$  TeV with the ATLAS detector*, (2021), arXiv: [2111.06606 \[nucl-ex\]](#).
- [10] J. G. Milhano and K. C. Zapp, *Origins of the di-jet asymmetry in heavy ion collisions*,  
[Eur. Phys. J. C \*\*76\*\* \(2016\) 288](#), arXiv: [1512.08107 \[hep-ph\]](#).
- [11] ATLAS Collaboration, *Measurement of jet  $p_T$  correlations in Pb+Pb and pp collisions at  $\sqrt{s_{NN}} = 2.76$  TeV with the ATLAS detector*, [Phys. Lett. B \*\*774\*\* \(2017\) 379](#), arXiv: [1706.09363 \[hep-ex\]](#).
- [12] ATLAS Collaboration, *Observation of a Centrality-Dependent Dijet Asymmetry in Lead-Lead Collisions at  $\sqrt{s_{NN}} = 2.77$  TeV with the ATLAS Detector at the LHC*,  
[Phys. Rev. Lett. \*\*105\*\* \(2010\) 252303](#), arXiv: [1011.6182 \[hep-ex\]](#).
- [13] CMS Collaboration, *Observation and studies of jet quenching in PbPb collisions at nucleon-nucleon center-of-mass energy = 2.76 TeV*, [Phys. Rev. C \*\*84\*\* \(2011\) 024906](#),  
arXiv: [1102.1957 \[nucl-ex\]](#).
- [14] ATLAS Collaboration, *The ATLAS Experiment at the CERN Large Hadron Collider*,  
[JINST \*\*3\*\* \(2008\) S08003](#).
- [15] M. Cacciari, G. P. Salam and G. Soyez, *The anti- $k_t$  jet clustering algorithm*, [JHEP \*\*04\*\* \(2008\) 063](#),  
arXiv: [0802.1189 \[hep-ph\]](#).

- [16] ATLAS Collaboration, *Luminosity determination in pp collisions at  $\sqrt{s} = 13$  TeV using the ATLAS detector at the LHC*, ATLAS-CONF-2019-021, 2019, URL: <https://cds.cern.ch/record/2677054>.
- [17] ATLAS Collaboration, *Operation of the ATLAS trigger system in Run 2*, JINST **15** (2020) P10004, arXiv: [2007.12539 \[physics.ins-det\]](#).
- [18] ATLAS Collaboration, *The ATLAS Collaboration Software and Firmware*, ATL-SOFT-PUB-2021-001, 2021, URL: <https://cds.cern.ch/record/2767187>.
- [19] ATLAS Collaboration, *Measurement of longitudinal flow decorrelations in Pb+Pb collisions at  $\sqrt{s_{NN}} = 2.76$  and 5.02 TeV with the ATLAS detector*, Eur. Phys. J. C **78** (2018) 142, arXiv: [1709.02301 \[nucl-ex\]](#).
- [20] C. Loizides, J. Kamin and D. d’Enterria, *Improved Monte Carlo Glauber predictions at present and future nuclear colliders*, Phys. Rev. C **97** (2018) 054910, arXiv: [1710.07098 \[nucl-ex\]](#), Erratum: Phys. Rev. C **99** (2018) 019901.
- [21] ATLAS Collaboration, *Measurement of  $W^\pm$  boson production in Pb+Pb collisions at  $\sqrt{s_{NN}} = 5.02$  TeV with the ATLAS detector*, Eur. Phys. J. C **79** (2019) 935, arXiv: [1907.10414 \[nucl-ex\]](#).
- [22] T. Sjöstrand et al., *An introduction to PYTHIA 8.2*, Comput. Phys. Commun. **191** (2015) 159, arXiv: [1410.3012 \[hep-ph\]](#).
- [23] ATLAS Collaboration, *ATLAS Pythia 8 tunes to 7 TeV data*, ATL-PHYS-PUB-2014-021, 2014, URL: <https://cds.cern.ch/record/1966419>.
- [24] R. D. Ball et al., *Parton distributions with LHC data*, Nucl. Phys. B **867** (2013) 244, arXiv: [1207.1303 \[hep-ph\]](#).
- [25] ATLAS Collaboration, *The Pythia 8 A3 tune description of ATLAS minimum bias and inelastic measurements incorporating the Donnachie–Landshoff diffractive model*, ATL-PHYS-PUB-2016-017, 2016, URL: <https://cds.cern.ch/record/2206965>.
- [26] S. Agostinelli et al., *GEANT4—a simulation toolkit*, Nucl. Instrum. Meth. A **506** (2003) 250.
- [27] ATLAS Collaboration, *The ATLAS Simulation Infrastructure*, Eur. Phys. J. C **70** (2010) 823, arXiv: [1005.4568 \[physics.ins-det\]](#).
- [28] M. Bähr et al., *Herwig++ physics and manual*, Eur. Phys. J. C **58** (2008) 639, arXiv: [0803.0883 \[hep-ph\]](#).
- [29] S. Gieseke, C. Röhr and A. Siódmok, *Colour reconnections in Herwig++*, Eur. Phys. J. C **72** (2012) 2225, arXiv: [1206.0041 \[hep-ph\]](#).
- [30] J. Pumplin et al., *New generation of Parton Distributions with Uncertainties from Global QCD Analysis*, JHEP **07** (2002) 012, arXiv: [hep-ph/0201195](#).
- [31] M. Cacciari, G. P. Salam and G. Soyez, *FastJet User Manual*, Eur. Phys. J. C **72** (2012) 1896, arXiv: [1111.6097 \[hep-ph\]](#).
- [32] ATLAS Collaboration, *Jet energy measurement with the ATLAS detector in proton–proton collisions at  $\sqrt{s} = 7$  TeV*, Eur. Phys. J. C **73** (2013) 2304, arXiv: [1112.6426 \[hep-ex\]](#).



- [33] ATLAS Collaboration, *Measurement of the azimuthal anisotropy of charged particles produced in  $\sqrt{s_{NN}} = 5.02$  TeV Pb+Pb collisions with the ATLAS detector*, *Eur. Phys. J. C* **78** (2018) 997, arXiv: [1808.03951 \[hep-ex\]](#).
- [34] ATLAS Collaboration, *Jet energy measurement and its systematic uncertainty in proton-proton collisions at  $\sqrt{s} = 7$  TeV with the ATLAS detector*, *Eur. Phys. J. C* **75** (2015) 17, arXiv: [1406.0076 \[hep-ex\]](#).
- [35] ATLAS Collaboration, *Jet energy scale and its uncertainty for jets reconstructed using the ATLAS heavy ion jet algorithm*, ATLAS-CONF-2015-016, 2015, URL: <https://cds.cern.ch/record/2008677>.
- [36] ATLAS Collaboration, *Measurement of photon-jet transverse momentum correlations in 5.02 TeV Pb+Pb and pp collisions with ATLAS*, *Phys. Lett. B* **789** (2019) 167, arXiv: [1809.07280 \[hep-ex\]](#).
- [37] G. D’Agostini, *A Multidimensional unfolding method based on Bayes’ theorem*, *Nucl. Instrum. Meth. A* **362** (1995) 487.
- [38] T. Adye, *Unfolding algorithms and tests using RooUnfold*, 2011, arXiv: [1105.1160 \[physics.data-an\]](#).
- [39] ATLAS Collaboration, *Jet energy scale measurements and their systematic uncertainties in proton-proton collisions at  $\sqrt{s} = 13$  TeV with the ATLAS detector*, *Phys. Rev. D* **96** (2017) 072002, arXiv: [1703.09665 \[hep-ex\]](#).
- [40] ATLAS Collaboration, *Measurement of jet fragmentation in Pb+Pb and pp collisions at  $\sqrt{s_{NN}} = 5.02$  TeV with the ATLAS detector*, *Phys. Rev. C* **98** (2018) 024908, arXiv: [1805.05424 \[nucl-ex\]](#).
- [41] ATLAS Collaboration, *Jet energy scale and resolution measured in proton–proton collisions at  $\sqrt{s} = 13$  TeV with the ATLAS detector*, *Eur. Phys. J. C* **81** (2021) 689, arXiv: [2007.02645 \[hep-ex\]](#).
- [42] W. Ke and X.-N. Wang, *QGP modification to single inclusive jets in a calibrated transport model*, *JHEP* **05** (2021) 041, arXiv: [2010.13680 \[hep-ph\]](#).
- [43] ATLAS Collaboration, *Measurements of the Nuclear Modification Factor for Jets in Pb+Pb Collisions at  $\sqrt{s_{NN}} = 2.76$  TeV with the ATLAS Detector*, *Phys. Rev. Lett.* **114** (2015) 072302, arXiv: [1411.2357 \[hep-ex\]](#).
- [44] CMS Collaboration, *In-medium modification of dijets in PbPb collisions at  $\sqrt{s_{NN}} = 5.02$  TeV*, *JHEP* **05** (2021) 116, arXiv: [2101.04720 \[hep-ex\]](#).